

Special Section:

Exploring planetary caves as windows into subsurface geology, habitability, and astrobiology

Key Points:

- A lava tube's strongest negative magnetic anomaly is correlated to tube geometry; specifically, cross-sectional area to depth to center
- The magnetic minimum gradients of a lava tube magnetic anomaly delineate the spatial position of the walls, indicative of lava tube width
- Lunar lava tube high spatial resolution magnetic observations can help establish viability for scientific exploration or human utilization

Correspondence to:

E. Bell,
ebell1@umd.edu

Citation:










Bell, E. Jr., Schmerr, N., Young, K., Esmaili, S., Garry, W. B., Jazayeri, S., et al. (2022). Field mapping and modeling of terrestrial lava tube magnetic anomalies as an analog for lunar lava tube exploration and prospecting. *Journal of Geophysical Research: Planets*, 127, e2021JE007140. <https://doi.org/10.1029/2021JE007140>

Received 23 NOV 2021
Accepted 7 MAY 2022

© 2022. The Authors.

This is an open access article under the terms of the [Creative Commons Attribution License](#), which permits use, distribution and reproduction in any medium, provided the original work is properly cited.

Field Mapping and Modeling of Terrestrial Lava Tube Magnetic Anomalies as an Analog for Lunar Lava Tube Exploration and Prospecting

Ernest Bell Jr.^{1,2,3} , Nicholas Schmerr⁴ , Kelsey Young² , Sanaz Esmaili⁵ , W. Brent Garry² , Sajad Jazayeri⁵ , Sarah Kruse⁵ , Jacob Richardson² , and Patrick Whelley^{1,2,3} 

¹Department of Astronomy, University of Maryland, College Park, MD, USA, ²Planetary Geology, Geophysics, and Geochemistry Laboratory, National Aeronautics and Space Administration Goddard Space Flight Center, Greenbelt, MD, USA, ³Center for Research and Exploration in Space Science and Technology, NASA/GSFC, Greenbelt, MD, USA, ⁴Department of Geology, University of Maryland, College Park, MD, USA, ⁵School of Geosciences, University of South Florida, Tampa, FL, USA

Abstract Lava tubes are a commonplace feature on the terrestrial planets, and knowledge of tube size and location informs lava flow processes. Future exploration of lava tubes on the Moon can provide access to geologic environments that likely remain unaltered from their emplacement billions of years ago. Lunar lava tubes may also provide astronauts protection from thermal extremes, meteoroid impacts, and radiation. High-resolution magnetic identification and characterization of lava tubes can be used to help inform future scientific investigations of lava tubes for human exploration and utilization. We demonstrate how magnetometry is useful for determining the geometry and extent of lava tubes on the Earth and, by proxy, the Moon, by relating the magnetic anomalies produced by lava tubes to their location and geomorphology. Using a proton-precession total field magnetometer, we surveyed an area of more than 100,000 m², with cross-tube linear traverses spaced at 3–5 m, perpendicular to an approximately 1,000 m length of the Modoc Crater lava tube complex, within the Lava Beds National Monument (California, USA). The observed magnetic anomalies of the sections known as Incline, Skull, and Ship Caves are compared against synthetic predictions, and the sensitivity of the magnetic anomalies to the tube geometry used to derive a basic relationship between the two. We use our model of terrestrial lava tube magnetic anomalies and adjust for the lunar magnetic environment to predict the signature of anomalies resulting from tubes on the Moon.

Plain Language Summary Lava tubes are caves that can form in flowing lava during volcanic eruptions and are suspected to also exist on the Moon. Lunar lava tubes could provide access to subsurface geologic features that are billions of years old, as well as provide shelter for future human lunar astronauts. Therefore, gaining a better understanding of the locations and sizes of lava tubes will be beneficial to future lunar exploration. Unfortunately, these caves are largely hidden within lava flows. So how can they be located and their size determined? Magnetometry is a geophysical method that uses measurements of magnetic field strengths to map locations of rock units. Solidified lava flows on Earth have magnetic fields that can be detected and quantified by specialized sensors. However, there have been few studies on the magnetic anomalies caused by lava tubes within lava flows. Our research examines the magnetic anomalies of lava tubes within the Lava Beds National Monument. We use observed data and detailed magnetic models to understand the practicality of mapping magnetic anomalies to determine lava tube locations and internal geometries within a lava flow. We also examine the ability to extend these techniques to locating and studying lava tubes on the Moon.

1. Introduction and Background

Future lunar exploration has the potential to lead to permanent human occupation of the Moon's surface. It is possible that the lava tubes could provide ideal locations for human lunar bases. They could afford human bases protection from radiation, extreme temperatures, and meteor impacts (Horz, 1985; Wendel, 2017). Beyond the possible use as safe havens for human lunar crews and hardware, exploration of lunar lava tubes has the potential to provide an increased scientific understanding of lunar volcanic and lava flow processes.

There exists a critical need for determining methods for locating and characterizing lava tubes to enhance the scientific and operational outcomes of future robotic and crewed missions (Titus et al., 2021). Areas to consider for searching for lunar lava tubes include locations extending along rilles and from apparent collapse pits (Wagner & Robinson, 2014) which have been identified as a high-priority landing target (Jawin et al., 2019). Other locations to search include areas containing lunar swirls, where the lines of the magnetic fields of lava tubes may be responsible for the variation in albedo in these regions (Hemingway & Tikoo, 2018), and may follow the lines of high or low magnetic gradient.

Existing standard methods to identify potential lava tubes include mapping the distribution of surface identified pits, which are interpreted to be skylights or collapses, in order to trace the pathway of lava tubes (Crown et al., 2019; Piombo et al., 2016). However, without a technique to probe the subsurface, there is no way to ensure the route of the lava tube, that the tube drained, or that the subsurface void space has not collapsed between skylights. Geophysical tools (gravity, magnetometry, and ground penetrating radar, etc.) have all proved promising for the detection and mapping of lava tubes on Earth and elsewhere (Esmacili et al., 2020; Haruyama et al., 2017; Mallozzi, 2019; Meglich et al., 2003; Miyamoto et al., 2005). Here, we specifically focus on the analysis of magnetic signatures to detect lava tubes and characterize their geometry. Magnetic data is relatively easy to collect at ground level over a lava tube and should provide the sensitivity to resolve the lack of material associated with the void of the lava tube within magnetically enriched basaltic lava flows.

1.1. Volcanism and Lava Tubes

Volcanism and associated lava flows are ubiquitous throughout the terrestrial bodies of the solar system, and play an important part in the formation and evolution of planets (Frankel, 1996; Sigurdsson et al., 2015), moons (Greeley, 1971a; Head, 1976), and large asteroids (Williams et al., 2014; Wilson & Keil, 1996). During a volcanic eruption, flowing lava can develop a type of cave, called a lava tube (Greeley, 1971b; Keszthelyi, 1995; Peterson et al., 1994; Sakimoto et al., 1997). Previous research indicates that lava tubes, with their thermally insulating characteristics, extend the transportation of subsequent lava away from its originating volcanic vent (Hon et al., 1994; Keszthelyi, 1995; Pieri & Baloga, 1986; Self et al., 1996; Walker, 1973) up to several kilometers further than channel-fed lava flows (Calvari & Pinkerton, 1998; Keszthelyi & Self, 1998). Lava tubes form when a flow of lower viscosity lava, typically mafic in composition, develops a solidified surface while maintaining an interior of flowing fluid lava. The formation mechanisms by which the surface solidification of the molten lava can occur in general includes the solidification of the crust of an inflating pahoehoe lava flow or the roofing over of an established lava flow channel, but in all cases this hardened surface provides an insulating layer for the molten lava that continues to flow underneath (Greeley, 1972; Hon et al., 1994; Peterson & Swanson, 1974a; Sauro et al., 2020). In the cases where the roof becomes structurally capable of supporting itself, and the molten lava drains from the enclosed interior, a hollow lava tube, or cave, is left behind within the solidified lava flow.

In the case of lava tube formation from an inflating lava flow, the flow front will consist of a series of overlapping lobes of lava that fuse and cool to form the roof of the lava tube (Greeley, 1971b; Peterson et al., 1994; Sauro et al., 2020). This mechanism generally occurs in slow moving lava flows and result in irregular constructs in comparison to tubes forming from continuous surface crusts (Greeley, 1971b). With this formation mechanism the surface skin of these lava tubes essentially cools and solidifies in place in comparison to some mechanisms of roofing of lava flow channels. These pahoehoe types of lava tube formations also have significantly more irregularity to their flow paths due to the unconstrained nature of the spreading of toes of the lava flow (Peterson et al., 1994).

Lava tubes originating from channel flows can be the result of several formation mechanisms. One possibility is for the crust to solidify along the channel edges via cooling and then grow toward the centerline of the channel, progressing downstream in a V-shape, essentially zippering over the channel (Greeley, 1971b; Peterson et al., 1994; Sauro et al., 2020). Another possibility, in channels with stable flow, is for the flow surface to develop a scum or crust. This initial roof thickens from either periodic overflow of flowing lava onto the surface or from an accretion of cooling lava on the underside of the surface layer, to the point of becoming structurally stable (Greeley, 1971b; Peterson et al., 1994). A third, similar formation mechanism to the previous, essentially constructs a roof from previously solidified crustal plates which have broken loose and been transported downstream. As these plates meet, they lock and fuse to the channel sides as well as to each other to create a roof across

the channel (Greeley, 1971b; Peterson et al., 1994; Sauro et al., 2020). These roof forming plates are therefore randomly orientated with respect to their orientation during cooling. A final process that can result in the creation of a lava tube from a channel occurs in more turbulent lava flows. In this case, the turbulence results in splashing, spattering, and lava overflow which create levees along the edges of the channel. These levees continue to conglomerate in an arch over the channel from each side, where they can eventually meet and fuse to form the roof of the lava tube (Greeley, 1971b; Peterson et al., 1994; Sauro et al., 2020).

When new lava flows inundate older tube-hosting flows, they may impact existing tube geometry by either elongating cross-sectional area or constructing a vertical stacking of multiple lava tubes on top of one another (Greeley, 1971b; Peterson et al., 1994). Internally, tubes may exhibit multiple levels that are indicative of when a flow resumed within a preexisting lava tube, but did not completely flood the previous tube, thus allowing for crusting of the new flow at an intermediate level within the established tube (Peterson & Swanson, 1974b; Peterson et al., 1994). Follow-on flows may also impact the current structure of a lava tube by causing a collapse of the tube, or by simply increasing the thickness of the roof. Long-lived tubes covered by multiple lava flows tend to lack evidence from which to determine the initial lava tube formation process, due to thermal erosion and annealing, which produces a surface glaze on most internal surfaces that hide growth structures (Peterson et al., 1994).

Many characteristic morphological features and structural modifications are found on or within lava tubes, including skylights, collapse features, and internal bridges or multiple levels/tubes. Skylights and collapse features are locations along the tube where the cave roof did not form or has been removed, forming holes, pits, or trenches with steep vertical walls in the local landscape (Arnold, 1986; Greeley, 1987). We define skylights as locations where the tube surface did not fully solidify, while collapse features are indicative that a portion of the tube has failed or slumped back into the tube. If lava tubes are not observed during formation, both of these types of openings are particularly important for recognizing the existence of a lava tube and are the primary morphology used for locating and tracing the paths of lava tubes (Piombo et al., 2016).

Terrestrial planets elsewhere in the Solar System are known to contain similar pit craters features associated with basaltic lava flows. These pit craters have been located on the lunar surface (Greeley, 1971a; Haruyama et al., 2009; Kaku et al., 2017; Sauro et al., 2020), as well as on the surface of Mars (Bleacher et al., 2017; Crown et al., 2019; Cushing et al., 2007; Sauro et al., 2020; Zhao et al., 2017). In some cases on the Moon these pits are indicative of more extensive subsurface void spaces that are interpreted as lava tubes based upon corroborating geophysical gravity (Chappaz et al., 2017) and radar sounding observations (Haruyama et al., 2017; Kaku et al., 2017).

1.2. Lunar Lava Tubes

Modern scientific discussion of the existence and formation of lunar lava tubes dates back to the NASA Apollo era (Greeley, 1971a). It has been suggested that Hadley Rille and other rille and rille-like structures within the Marius Hills region are lava channels or partially collapsed lava tubes (Greeley, 1971b; Hurwitz et al., 2013; Keszthelyi, 1995; Roberts & Gregg, 2019). In addition, there have been over 150 pit craters identified on the lunar surface from the Lunar Reconnaissance Orbiter (LRO) data (Robinson et al., 2012; Wagner & Robinson, 2014, 2021). These pits are located at various mare and melt pond regions including Mare Ingenii, Mare Tranquillitatis, King pond bridge, and the Copernicus pond pit. Due to the lack of ejecta or volcanic deposits these pits appear to be either skylights or collapsed roofs of lava tubes and magma chambers (Head & Wilson, 2017; Robinson et al., 2012). While most of these pits are likely shallow (<10 m), it is probable that several provide access to lava tube systems (Wagner & Robinson, 2014) as well as to emptied near-surface magma conduits (Halliday, 1998; Robinson et al., 2012).

The first of these pits was discovered in the Marius Hills region (Haruyama et al., 2009). This specific pit, known as the Marius Hills Hole (MHH), shown in Figure 1c, is an average 65 m in diameter and has a depth from lunar surface of between 80 and 88 m, with an original roof thickness of at least 40 m (Haruyama et al., 2009; Robinson et al., 2012; Wagner & Robinson, 2014). A large number of sinuous rilles are located within the Marius Hills region, including the 32+ km long rille, Rille A, on which the MHH pit is located (Robinson et al., 2012). It is feasible that some lunar lava tubes are orders of magnitude larger than their terrestrial counterparts. Structural analysis shows that they may be up to several kilometers in diameter, which is on the scale of sinuous rilles found

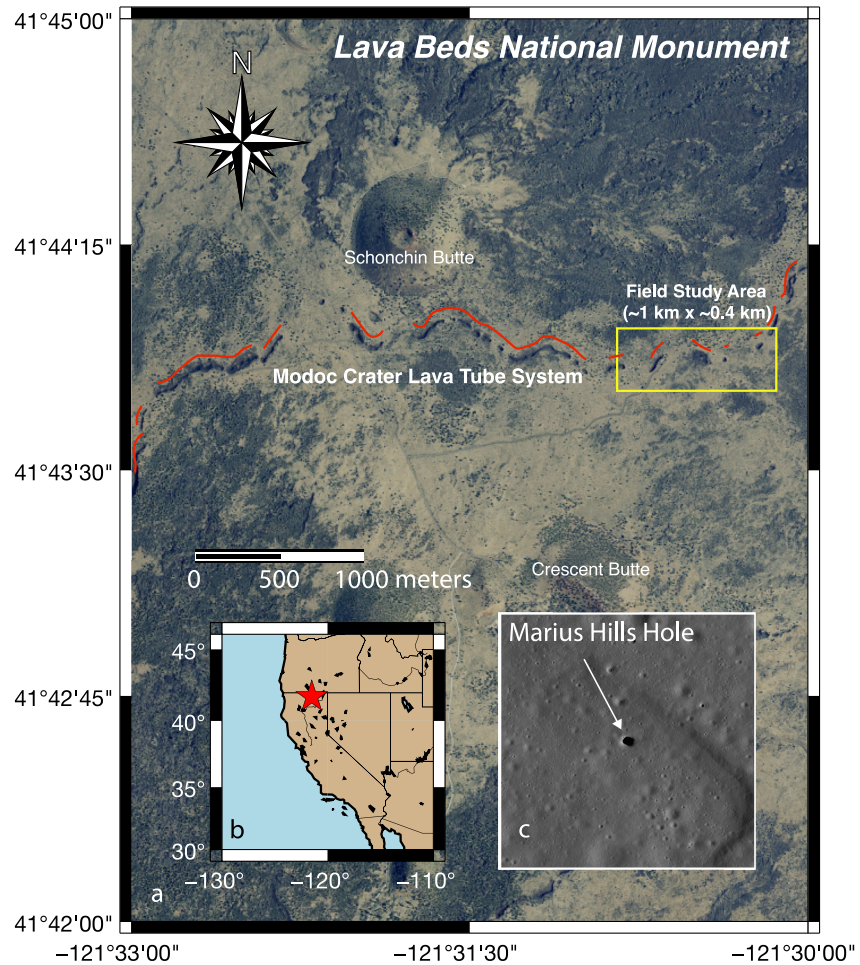


Figure 1. (a) Aerial view of Lava Beds National Monument (LBNM) showing the location of Modoc Crater lava tube complex (red tracing next to visually identifiable collapsed pit features), and the location of our field study area (seen in Figures 2 and 3) indicated with a yellow box. Basemap: National Agriculture Imagery Program orthomosaic. (b) LBNM location in northern California. (c) Image showing Marius Hills Hole, a collapsed pit suspected to lead to a lava tube on the Moon (located at 303.3°E, 14.2°N). Hole diameter is approximately 65 m, and image is at the same scale as Figure 1a. LROC NAC image: M114328462R.

on the Moon (Blair et al., 2017). Along this line, it is projected that Rille A contains a lava tube with a width of 370-m-wide based on the observed dimensions and depth of the MHH, and an estimated tensile strength of 6.9 MPa and density of 2,500 kg/m³ for the basalt (Haruyama et al., 2009). This estimated width results in a plausible lava tube geometry for this location that is greater than the diameter of the MHH and less than the approximately 500-m-wide rille (Haruyama et al., 2009).

Recent geophysical investigations using lunar orbital mission data further support the interpretation that the MHH leads to a lunar lava tube, though these findings are not yet definitive. In one study, gravity data from the GRAIL spacecraft was used to determine that the Marius Hill region contains several lines of mass deficit, including one that intersects the MHH (Chappaz et al., 2017), though the gravity anomaly colocated with MHH is much broader than the estimated size for the potential tube. Additionally, radar evidence from the SELENE Lunar Radar Sounder indicated a possible cave-like void extending from the MHH (Kaku et al., 2017), though subsequent analysis concluded that void space detections were actually echoes from surface clutter and not from the voids of lava tubes (Kobayashi et al., 2021). Therefore, work remains to conclusively determine the existence and locations of lava tubes on the Moon.

1.3. Terrestrial and Lunar Magnetic Studies

Magnetic methods have long been used to measure and map volcanic units with a magnetic signature (George et al., 2014; Marshall et al., 2015), or in the case of tubes, detecting the lack of magnetic signal from a cavity or void space against a rock with a magnetic signal (Burger et al., 2006; Mallozzi, 2019; Meglich et al., 2003). Magnetic techniques have adequate resolution to reveal various subsurface magmatic structures on Earth (George et al., 2014; Negro & Ferrucci, 1998), and have provided magnetic maps of the continents and seafloor (Hinze & Hood, 1998; Klitgord et al., 1975; Minty et al., 2003).

Early orbital missions to the Moon (Dolginov et al., 1963, 1966) found no evidence of a present-day magnetic field, though Luna 10 first identified potential surface anomalies, indicating a paleofield (Dolginov et al., 1966). During the Apollo program, surface magnetometers were used, including stationary locations on Apollo 12, 14, 15, and 16, as well as portable units on Apollo 14 and 16 (Dyal & Gordon, 1973). The results of the seven data points recorded by the handheld units on Apollo 14 and 16 show a variation in absolute magnetism from 40 to 313 nT, with a maximum gradient of 370 nT/km in Descartes and 54 nT/km in the Fra Mauro (Dyal & Gordon, 1973). These magnetometers confirmed the lack of a current magnetic field as well as the presence of magnetizing fields during the formation of geologic units at each landing site.

More recently, the Lunar Prospector orbiting spacecraft recorded the distribution and strengths of magnetic anomalies on the lunar surface (Binder, 1998; Ravat et al., 2020; Tsunakawa et al., 2010, 2015). Many of these anomalies are suspected to be associated with impactor or ejecta material (Hood et al., 2001; Wiczeorek et al., 2012). There is also some correlation between a group of magnetic anomalies, on the nearside, with the Rima Sirsalis extensional graben, that would support the theory that the sources of the anomalies are subsurface igneous intrusions (Hood et al., 2001; Srnka et al., 1979). Recently, Hemingway and Tikoo (2018) discussed the possibility of lunar lava tubes accounting for the existence of lunar swirls. They postulated that lunar lava tubes may have provided the mechanism for increased magnetic anomalies of the surrounding basalts by imparting a thermoremanent or thermochemical remanent magnetization.

Magnetic anomalies produced by lava tubes are due to the void space they create within the lava flows within which they reside. Basaltic lava flows are inherently magnetic due to containing appropriate mineralogy to have both remanent and induced magnetic properties. The remanent magnetic properties are set in the ferromagnetic matrix of the basalt during cooling below the Curie point, the temperature below which materials lock-in a permanent magnetic set if cooling within a magnetic field, such as the Earth's, or the past lunar, dipole magnetic fields.

Although there is no current lunar dynamo, a global magnetic field of $\sim 77,000$ nT previously existed until declining to a magnitude of $5,000 \pm 2,000$ nT by ~ 3.2 Ga (Strauss et al., 2021; Tikoo et al., 2017). This lower level field has been shown to have existed until between 2.5 and 1.0 Ga (Strauss et al., 2021; Tikoo et al., 2017). This timeframe includes the period of the major basin forming events and lunar volcanism which occurred between approximately 3.9 and 2.5 Ga (Head, 1976; Hiesinger et al., 2010). From studies of lunar samples returned during the Apollo missions it is known that, although different from Earth, the Moon contains sufficient compositional percentage of ferromagnetic material to provide observable magnetic signatures (Nagata et al., 1974). The composition includes both metallic iron, Fe-Ni-Co alloy dominated by Fe, and kamacite, with the kamacite theorized to be partially of meteoric origin. Studies have found that lunar samples can contain thermoremanent magnetization (Doell et al., 1970; Runcorn et al., 1970). Although the lunar magnetic field may have been an order of magnitude less than the Earth's current magnetic field during the period of time of the majority of lunar volcanism, the presence of a magnetic field of approximately 5,000 nT on the Moon would have provided the mechanism for the basalt forming lunar lava tubes to acquire a remanent magnetic signature during emplacement (Strauss et al., 2021; Tikoo et al., 2017).

However, there are few examples of research that have been conducted on the correlation of lava tube magnetic anomalies and their specific geomorphologic characteristics. Terrestrial examples have included validating the use of magnetometry for determining the presence of a lava tube under a roadway within Lava Beds National Monument (LBNM) (Meglich et al., 2003), as well as attempts to track lava flows within active lava tubes, using thermomagnetic effects, during the 1991–1993 Mount Etna eruption (Budetta & Negro, 1995). Both studies showed that magnetometry can provide details on lava tube location, depth, and size. However, a more general model that relates these features to tubes of different geometries remains to be developed. This is because

inverting for the structure of an underlying magnetic anomaly does not necessarily produce a unique solution, and the complexity of natural lava tube systems necessitates a sufficiently high-resolution survey over the tube structure.

Here, we develop an observationally derived relationship between tube geometry and magnetic signature of lava tubes by combining a systematic magnetic survey and ground reference data provided by Light Detection and Ranging (LiDAR) scans of tube geometry. LiDAR scans were also used to construct three-dimensional models to calculate the idealized magnetic signature of each lava tube. We then apply our results to make predictions for the magnetic signatures of lava tubes expected on the Moon. To our knowledge, there has not been a dedicated study of the correlation of magnetic anomaly to lava tube locations and morphology on either the Earth or the Moon. Our study of a tube system on Earth is designed to extrapolate to the Moon by connecting high-resolution (~ 5 m scale) ground-level magnetic signatures over a lava tube with known subsurface lava tube morphology to test if a scaling relationship can be used to infer lava tube structures elsewhere in the Solar System. These results are expected to have practical application in the research of lava tubes in both terrestrial lava fields and for future lunar exploration.

2. Geologic Setting: Lava Beds National Monument

In this study we specifically focus on terrestrial lava tubes within LBNM, California, USA and relate our results to lunar lava tube structures. The LBNM encompasses a multitude of lava tubes, lava flows, and cinder cones that are associated with the Medicine Lake shield volcano (Figure 1). The Medicine Lake volcano is located near the border of California and Oregon and is the largest volcano (Donnelly-Nolan, 2010; Larson & Larson, 1990) within the Cascade Range, covering an area of over 2,000 square kilometers (Donnelly-Nolan, 2010). Volcanic eruptions have occurred here for over the past 500,000 years, forming over 200 volcanic vents sourced from multiple magma chambers (Donnelly-Nolan, 2010).

Most of the lava tubes, including those used in this study, found within LBNM are from basaltic flows that occurred 36 ± 16 ka from the Mammoth and Modoc volcanic craters on the southern border of the monument (Donnelly-Nolan, 2010). The most recent lava flows occurred at 12 ka in the southeast corner of the monument (Donnelly-Nolan, 2010). In total, dozens of lava flows are contained within the LBNM, stemming from periodic eruptions every few hundred to several tens of thousands of years (Donnelly-Nolan, 2010).

LBNM contains the greatest number of lava tube cave entrances, over 200, within the continental United States (Larson & Larson, 1990). The resulting intact lava tube caves range in length from just a few meters to approximately 7,000 m of surveyed passageways. The complexity of the tube systems also varies from simple single passageways to multiple vertical levels and/or interwoven horizontal branches. Many of the more notable caves within LBNM have infrastructural improvements, including clearing of some ceiling collapses to create pathways and the installation of ladders for public access, but the tubes in this study do retain their primary morphologic features and structural characteristics (Larson & Larson, 1990).

Our study surveys three adjacent intact sections of the Modoc Crater lava tube network (Figure 2). The Modoc Crater network of lava tubes is approximately 16 km in length and is interpreted to be formed by a roofed over trench lava flow (DeDecker, 2014). The westernmost cave in our study, Incline Cave (western entrance, 41.7307°N 121.5136°W) is a single-level cave located at the western extent of a collapsed trench that connects Incline and Skull Caves. The western opening is easily located (Figure 2b). Skull Cave (entrance, 41.7314°N , 121.5107°W) is an exceptionally large diameter (primary portion is $\sim 18\text{--}20$ m), multi-level lava tube. Features within the tube include extensive collapsed ceiling and wall blocks of meter scale, some of which exhibit examples of solidified pahoehoe flow and rope features (Arnold, 1986; Larson & Larson, 1990). Its western entrance is shown in Figure 2c. Ship Cave (entrance, 41.7311°N , 121.5060°W) is located further down flow from Skull Cave and is separated from Skull Cave, from west to east, by a large collapsed trench and two intact but unconnected caves within the Modoc Crater tube system. Ship Cave is accessed via a roughly circular, ~ 24 m diameter collapsed pit positioned between it and Dinghy Cave to the west. Figure 2d provides a picture of the internal view of Ship Cave, looking west toward its entrance.

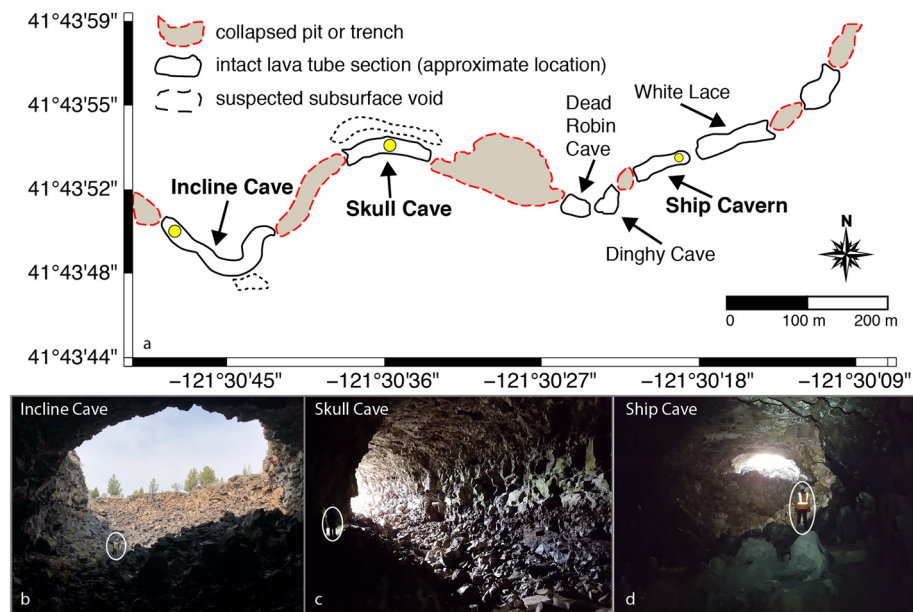


Figure 2. (a) Schematic depiction of the Modoc Crater lava tube complex field area in yellow box from Figure 1. Locations of the three analyzed caves (Incline, Skull, and Ship) are noted in bold text. (b) View looking out of Incline Cave toward the collapsed trench at the western entrance. Photograph credit: Jacob Richardson. (c) View from inside of Skull Cave looking toward the cave entrance to the west. The floor is littered with significant ceiling and wall collapses. (d) View from inside of Ship Cave looking west toward the cave entrance. The floor is lined by large meter-scale basaltic blocks collapsed from the ceiling and walls. For reference, ~1.8 m tall person, is circled in panels (b–d). Approximate location of pictures denoted by yellow dots in each cave.

3. Methodology

For our methodology, we collected and processed both ground level total field magnetic surveys over the lava tubes, and three-dimensional LiDAR point cloud surveys of the interior of the lava tubes as well as the ground level topography. Using this data, we created forward models of the theoretical magnetic anomalies produced by the lava tubes and determined the ground level magnetic gradients for both the observed and synthetic data.

3.1. Field Data Collection and Processing

3.1.1. Ground Level Magnetic Survey

To record the total magnetic strength above the lava tube complex, we used a GEM Systems (Geophysical Electromagnetic Systems) GSM-19 Overhauser magnetometer (GEM Systems, Inc., 2008) during two separate field seasons in May 2017 and September 2018. The magnetometer system acquired the total magnetic field strength at a resolution of 0.2 nT with an absolute accuracy of 1 nT at 5 Hz (GEM Systems, Inc., 2008). The magnetometer was deployed 2 m above the ground on a boom attached to a non-magnetic backpack. The magnetic data was collected by performing ground level magnetic surveys with continuous data acquisition, acquired at 5 Hz. Carried at walking speed, this corresponded to an average along-track spacing of <0.2 m between readings. Quasi-parallel lines were walked perpendicular to the tube direction as determined from U.S. Geological Survey Maps (Waters et al., 2010), and were pre-mapped on a handheld GPS unit at 2-m to 4-m intervals. We typically extended the lines ~20–50 m to either side of the estimated location of the walls of the lava tube being surveyed. The GPS location for each data point was also recorded, as deviations around sagebrush and other obstacles were routinely necessary. In total, approximately 100,000 m² along a 1 km length of the Modoc Crater Lava Tube complex were surveyed (Figure 3) (Bell et al., 2018, 2020).

Some areas, such as north of Ship Cave were not surveyed due to hazardous walking conditions and/or obstruction by dense vegetation.

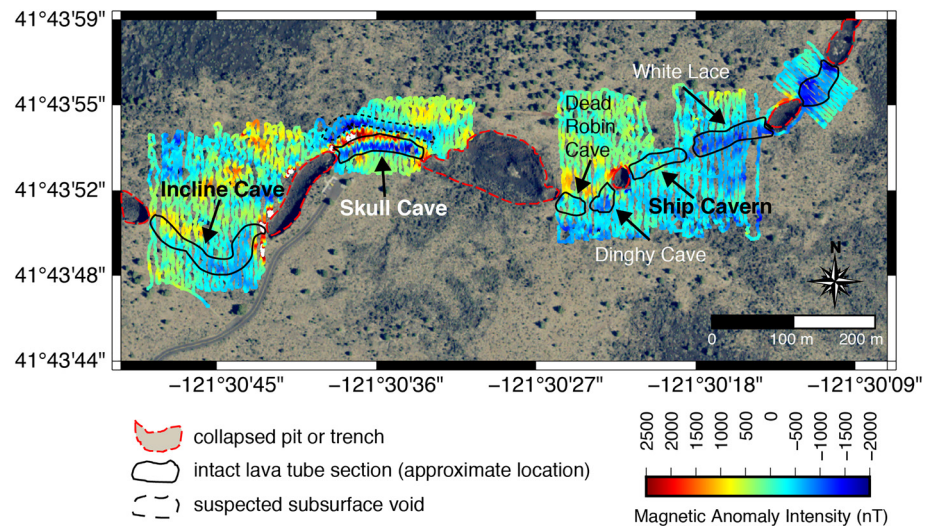


Figure 3. Ground level surface magnetic anomaly survey of a portion of the Modoc Crater lava tube system. Lava tube subsurface perimeters are shown in the black outlines. Collapse pits are indicated by broken red lines, and the magnetically inferred location of an unexplored subsurface tube is in broken black lines. Magnetic field is reported relative to the local background (50,685 nT at Skull Cave segment, and 50,541 for all other segments), and the color bar saturates to white at +2,500 and black at −2,000 nT. Background aerial image credit: National Agriculture Imagery Program orthomosaic.

To remove the background magnetic field of the Earth we used the International Geomagnetic Reference Field model from the NOAA National Center for Environmental Information (NCEI) Magnetic Field Calculators for the total magnetic field intensity for LBNM on the days of the surveys. The total field average was 50,685 nT for the 1 May 2017 observations around Skull Cave, and 50,541 nT for the September 6–8, 2018 observations of Incline and Ship Caves (National Geophysical Data Center, 2020). Figure 3 presents the resulting magnetic anomaly map created from the observed ground level magnetic survey of our field area portion of the Modoc Carter Lava Tube complex after these corrections were applied.

We concluded that corrections for diurnal variations did not need to be applied to our data set owing to the low diurnal variation during the data acquisition time relative to the overall background magnetic variation across the lava flow itself. We evaluated the average diurnal variation in the total Earth magnetic field recorded at the three USGS Geomagnetic Observatories (Fresno, CA; Newport, WA; & Tucson, AZ) closest to LBNM during the dates overlapping our magnetic surveys. The largest diurnal variation gradient was 7.5 nT per hour over 2 hr and 17 min, on 7 September 2018, during a portion of the Ship Cave magnetic survey. For the same location the background variation due to the lava flow is ± 281 nT, which is also the lowest background variation of the three lava tubes. For the rest of the data collection, the largest diurnal variation was between 2 and 4 nT per hour.

For our magnetic analysis of Incline, Skull, and Ship Caves, we selected the data points from the areas surrounding each respective tube (Figure 4). Data points were then interpolated onto a regular 1-by-1-meter grid and smoothed by performing a 5-by-5-meter median filter, selected due to the original 3–5 m spacing of the survey lines. We then removed the median observed background variation, of −13.15 nT, created by the basaltic lava flows surrounding the lava tubes from the NOAA NCEI model.

3.1.2. Three-Dimensional Laser (LiDAR) Surveys

Multiple LiDAR 3D surveys were completed of both the interior of the lava tubes and the overlying ground surface topography with a Riegl VZ-400 tripod mounted terrestrial laser scanner (Garry et al., 2017; Whelley et al., 2018). The LiDAR data captures sub-centimeter geomorphologic details of the interiors and ground level topography. Data from outside of the tube were geo-located using a pair of high accuracy differential GPS receivers. LiDAR data from the tube interiors, where GPS satellite lock was not possible, were then merged with outside scans in RiSCAN Pro 2.8 software. The resulting point cloud provides geometry, locations, and distances from the surface to any feature of interest and a three-dimensional map of the interior of the lava tube with a

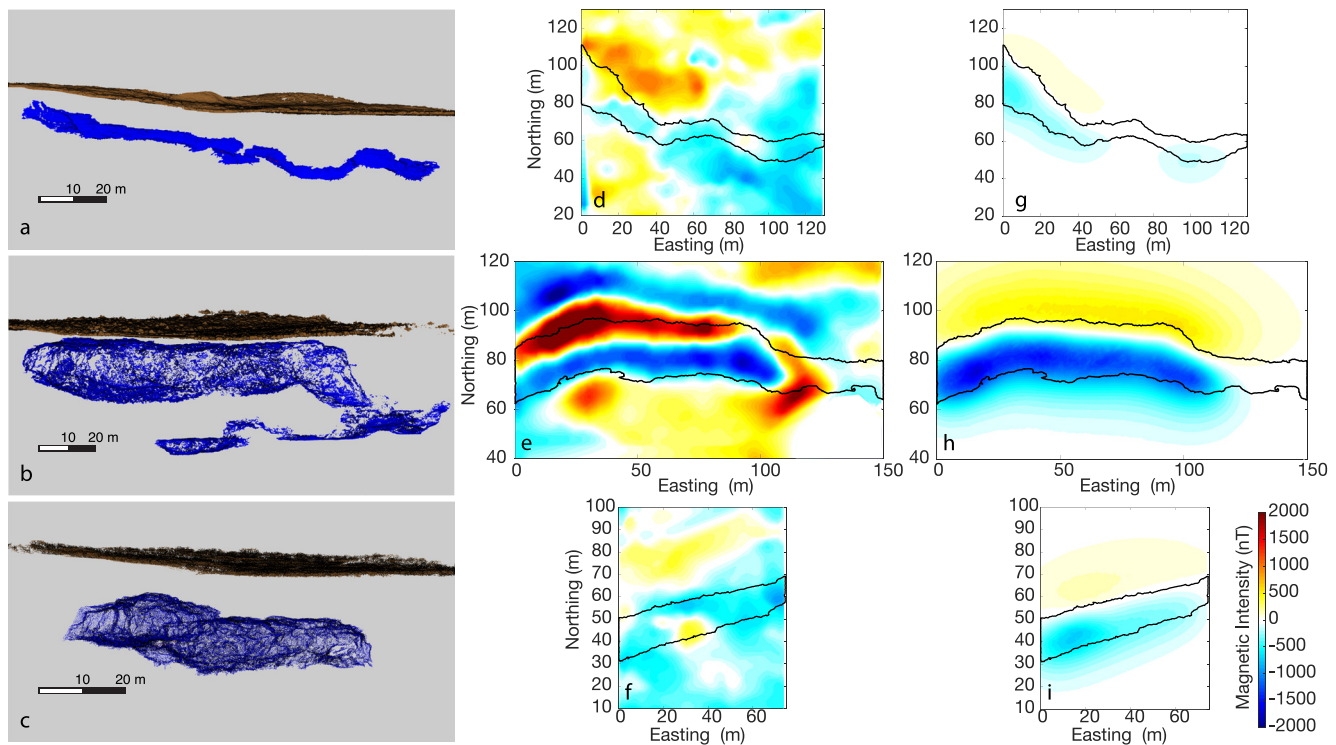


Figure 4. Orthographic view of downsampled 10-cm point-spacing LiDAR point cloud models for (a) Incline, (b) Skull, and (c) Ship caves for the corresponding outlined perimeters shown in black in the aerial plots of the observed magnetic anomalies (plots d–f), and the modeled magnetic anomalies (plots g–i) for the same recorded portions of the lava tube caves assuming a uniform effective susceptibility of 0.155 in the subsurface.

cm-accurate relation to the ground surface topography. The high-resolution LiDAR data scans were produced for the three intact tube portions, Incline, Skull, and Ship Caves shown in Figures 4a–4c.

The original sub-centimeter point spacing LiDAR point cloud surveys were down-sampled to 10-cm point spacing using CloudCompare (Girardeau-Montaut, 2016). This enabled the extraction of surface topography and lava tube interior points within a rectangular prism surrounding each lava tube.

From these reduced LiDAR point clouds, we generated finite point models, with regular spacing, for use in calculating theoretical idealized 2D magnetic anomalies produced by the lava tubes and surface topography. To complete this regularizing of the point cloud spacing, a 3D grid was defined with 1-m spacing between points in the easting direction (along the general longitudinal axis of the lava tube), 0.25 m spacing in the northing direction, and 0.25 m spacing in the vertical direction. Then from the LiDAR data each point on this regular grid was defined as being either inside or outside the lava tube. For the surface topography, the elevations of the LiDAR surface topography were interpolated onto the same 1-m easting and 0.25 m northing grid. These uniformly spaced point models of the lava tubes and topography allowed for the construction of parameterized 3D grid elements for models of the desired resolution.

3.2. Magnetic Modeling

The 3D-grid point models described above were used to create forward models of the expected magnetic signatures of the lava tubes. In these regularized models we assigned rectangular prismatic dimensions of $1.0 \times 0.25 \times 0.25$ m, in X (easting), Y (northing), and Z (vertical) directions to each point on the grid. We then assume the surrounding basalt is homogeneous and assigned a constant magnetic susceptibility of 0.155 to all prisms inside the lava tube, for reasons described below.

As we do not have an independent constraint on induced versus remanent magnetism, we set the remanent magnetism to zero, and performed the initial analysis assuming an effective magnetic susceptibility accounts for both the induced and remanent magnetism. For this, we prescribed the Earth's field direction at LBNM,

with magnetic inclination 64.7° and declination 14.3° . The effective magnetic susceptibility value of 0.155 was derived from our results described in the following sections. We applied properties only to the prisms inside the lava tube void to minimize the required number of prismatic elements and reduce the forward modeling computational time. The resulting amplitudes were then phase shifted by 180° (multiplied by -1) to determine the proper magnetic anomaly signature produced from the absence of basaltic material in the lava tube void. This method also removed the edge effects of the magnetic field from the boundaries of a modeled block of basalt from interacting with a lava tube void within it in order to isolate the model to the effects of the void itself within infinite block of basalt.

Our prismatic element model was then processed with a modified version of the “GRAV_MAG_PRISM” Matlab® script to compute the magnetic signature of these rectangular prismatic elements (Bongiolo et al., 2013). The Matlab code generates the synthetic two-dimensional ground surface magnetic signature, at a desired elevation, with the magnetic anomaly strength for a surface observer at each point being the summation of all the elements in the model (Bongiolo et al., 2013). For our models, the final results are equivalent to the lava tubes' magnetic anomalies as observed from the sensor height of 2 m above the ground.

To reduce computational requirements, the original code assumed that all prismatic bodies were located beneath a flat surface at $Z = 0$. The expression for the total magnetic anomaly produced by a rectangular prismatic body (Bongiolo et al., 2013, Equation 33), is

$$\Delta T(x, y, 0) = G_1 \ln F_1 + G_2 \ln F_2 + G_3 \ln F_3 + G_4 \ln F_4 + G_5 \ln F_5 \quad (1)$$

where ΔT is the total field anomaly at $z = 0$, and the constants G_1, G_2, G_3, G_4 , and G_5 are a combination of the magnetization vector, direction cosines of magnetization, and the directive cosines of the geomagnetic field environment as described in Bongiolo et al. (2013). The constants F_1, F_2, F_3, F_4 , and F_5 are a representation of the coordinates of the vertices of each prismatic element used to locate each prism within the geomagnetic field (Bongiolo et al., 2013). Together they are used to calculate the total magnetic field created by each individual prismatic element. These individual results for each prism are then combined to determine the total magnetic intensity at each point on the surface ($Z = 0$). We introduced a modification into the Matlab script that accounts for the variation in elevation of the actual surface topography above the lava tubes. Our script modification provides for a better synthetic magnetic anomaly signature with which to compare our field observations. The modification sets the highest elevation of the ground surface, for the area being analyzed, equal to $Z = 0$. The rest of the points in both the ground topography and lava tube point clouds are then vertically referenced to this location. The difference between the $Z = 0$ elevation and the maximum elevation at each X – Y location in the regularized ground topography point cloud is then calculated, creating a two-dimensional matrix of the topographic variation for the area above the lava tube. This vertical topographic variation difference is then removed from the depth to each of the regularized lava tube point cloud points for each X – Y position. Essentially this adjusts the depths of all the lava tube prisms toward the surface to their same absolute depths below what would be a flat plane located at the $Z = 0$ location of the ground topography, where:

$$h_{\text{equivalent}} = h_{\text{maximum}} - h_{\text{topography}} \quad (2)$$

Implementing this modification results in additional computations for each X – Y location to determine the modified depth, $h_{\text{equivalent}}$, to each of the lava tube prisms, but creates a magnetic signature across a flat plane at $Z = 0$ that accounts for the relative depth of the lava tube beneath the actual undulating topography located above the lava tube. The final resulting magnetic anomaly maps for our models of the three lava tubes, Incline, Skull, and Ship Caves, are shown in Figures 4g–4i.

3.3. Calculation of Magnetic Gradients

Along with the previously described analysis, ground-level surface gradients of the magnetic field were calculated using both the observed data and the synthetic models. Calculation of magnetic gradients is one method used to examine magnetic survey data to determine the geometry of the source of a magnetic anomaly. Maxima or minima in gradients tend to outline the edges of sources (Ferreira et al., 2013). The magnetic gradients for our study are calculated by applying a standard Sobel operator (Duda et al., 1973; Sobel, 2014) which is a weighted sum of adjacent pixels, or points, regularly used to detect edges in image processing. It first calculates the

Table 1
Summary of Lava Tube Geomorphology

	Accessible length (m)	Height of primary section (m)	Width of primary section (m)	Ceiling depth of primary section (m)
Incline Cave	>130	1–10	1–30	5–24
Skull Cave	>180	5–20	5–20	6–35
Ship Cave	>100	6–7	12–19	7–15

latitudinal and longitudinal components of the gradient at each of the points on the magnetic anomaly map. The gradient magnitude is then computed by taking the square root of the sum of the squares of the components at each data point for the magnetic anomaly map. For data at map edges, the values outside the boundary of the magnetic anomaly map are assumed to be equal to the nearest anomaly map value.

4. Results

The results of the analysis of our field and modeled data sets provide for examination of the geomorphology of the three lava tubes studied, as well as the lava tube magnetic anomaly signatures and gradients.

4.1. Geomorphology of Incline, Skull, and Ship Caves

Field observations and lidar surveys collected as a part of this study enabled an in-depth examination of the morphologies of each cave of interest. Point cloud perspective views of each cave are provided in Figure 4 and gross dimensions of each cave are summarized in Table 1.

Incline Cave is approximately 130 m in length starting with an oval-shaped cross section, approximately 10 m high by 30 m wide, at its western opening. The depth below ground surface to the ceiling of Incline Cave increases from 5 m at this opening to approximately 24 m at its eastern extent where it connects to the trench leading to Skull Cave. Along this transect from western end to eastern end the cross-sectional area decreases to just a few square meters. The interior consists of extensive blocks, of meter scale, collapsed from the walls and ceilings. The reduction in cross-sectional area is partly due to increasing collapse within the tube from west to east.

Skull Cave is approximately 180 m in length, with a maximum depth below ground surface to the ceiling of about 36 m. Skull Cave has the largest diameter of all three tubes (primary portion is ~18–20 m) and has multiple levels. The intact portion of the tube we surveyed is located between two collapsed trenches, each greater than 120 m in length. The trench to the west, or up flow, of Skull Cave, is approximately 23 m wide, and the downstream trench to the east is approximately 40–50 m wide. The depth-to-ceiling is between approximately 6 and 8 m from the western entrance until about 115 m into the cave, at which point it increases rapidly in depth as the cave constricts and drops to a lower level with a depth-to-ceiling of 30–35 m below ground level. Skull Cave's uppermost level ends some 125 m inside, at which point there is a collapse into a lower level. The lower level continues approximately 50 m further on down flow, with access also extending back up flow, in the direction of the cave entrance, underneath the upper level for about 80 m. This 80 m section features significant perennial ice accumulation. Additionally, at the furthest reaches of Skull Cave, there is a breach on the south side of the tube exposing welded and oxidized material.

Ship Cave is a relatively large intact portion of the tube system of fairly consistent cross section, ~19 m wide by 7 m high at the entrance and gradually constricting down to a width of 12 m and height of 6 m at the farthest extent. The depth-to-ceiling is ~7–8 m near the entrance, dropping to ~15 m at the down flow end of the cave. The furthest reach appears to be blocked by a combination of collapse and solidified basaltic flow. As in Skull and Incline caves, features consist of significant collapse of the ceiling and wall lining resulting in meter scale blocks covering the floor.

4.2. Magnetic Signatures of Incline, Skull, and Ship Caves

Figures 4d–4f illustrate the final smoothed and filtered plots of the magnetic anomalies for each of the three lava tubes at approximately 2 m above ground level. Magnetic anomalies are most pronounced at Skull Cave, where the magnetic field varies by 4,000 nT. At Incline and Ship Caves, magnetic anomalies have lower amplitudes, with field variation of ~2,000 nT or less. All three caves exhibit a common magnetic pattern, where lower magnetic field values are found within the plan view extent of each tube and a positive magnetic anomaly runs to the north, parallel to each tube. This is most clear at Skull Cave and in the western extent of Incline cave, and less clear at tube sections of smaller diameter or increased overburden (eastern Incline Cave and Ship Cave). In addition to this consistent pattern, an additional negative anomaly runs parallel to Skull Cave along its north side.

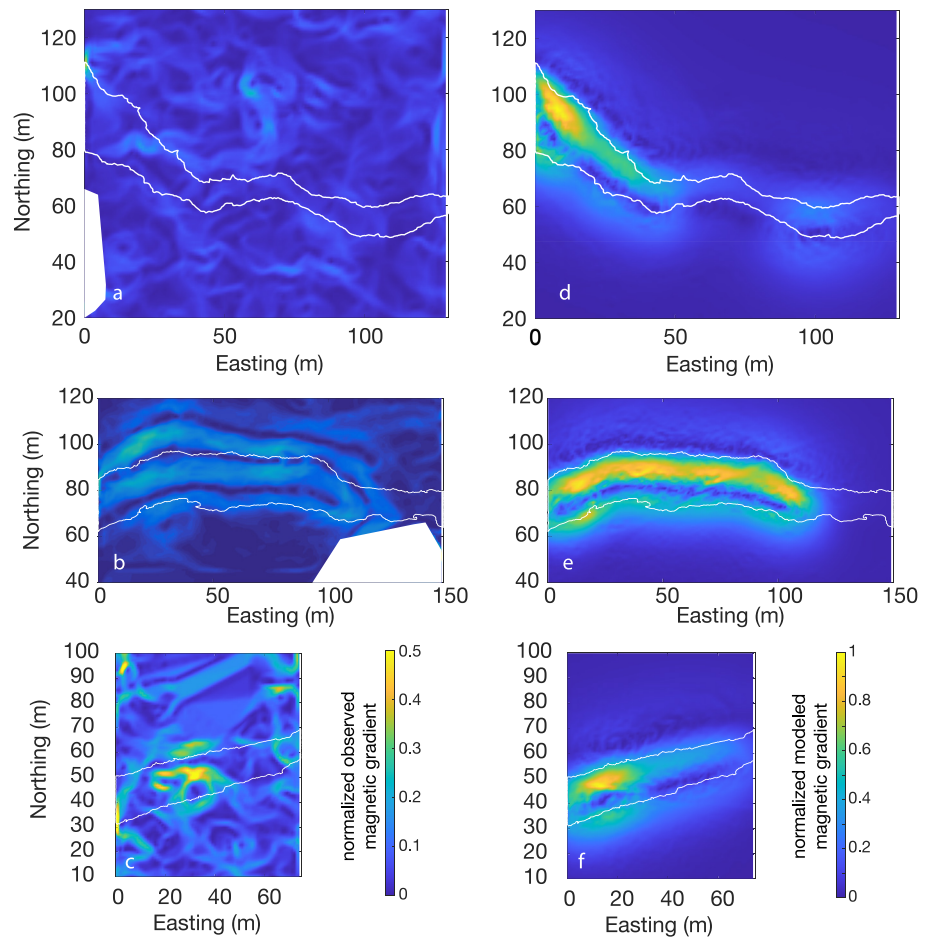


Figure 5. Normalized magnetic gradient plots for both the observed (left column) and modeled (right column) magnetic gradient plots of (a and d) Incline, (b and e) Skull, and (c and f) Ship lava tube caves, respectively. LiDAR derived lava tube perimeters are outlined in white. Magnetic gradients plotted are normalized to the highest gradient (nT/m) calculated for each figure.

Gradient plots of the observed and modeled magnetic fields of each tube are shown in Figure 5. In the plots of the observed magnetic gradient data, the Skull Cave (Figure 5b) perimeter is outlined by lines of minimum magnetic gradient, whereas Incline Cave (Figure 5a) and Ship Cave (Figure 5c) perimeters are obscured by additional gradient lines from localized anomalies. In the plots of the magnetic gradients from the modeled magnetic anomaly data, the LiDAR derived outline of the tube perimeters of all three lava tubes are consistently ~ 5 m south of the minimum magnetic gradients, seen in Figures 5d–5f.

5. Discussion and Interpretation of Results

From our results, we relate the observed magnetic anomalies produced by lava tubes to those modeled by a buried cylindrical rod to understand the relationship between the geometric ratio of the cross section of a lava tube to the strength of the magnetic anomaly. We describe the utility of the magnetic gradient for interpreting the location and geometry of a lava tube, and discuss the similarities and differences between the observed and modeled magnetic anomalies of lava tubes. This is followed by a description of the possible identification of a previously unknown lava tube location at LBNM. Finally, we describe extending this approach to locating and characterizing lava tubes on the Moon.

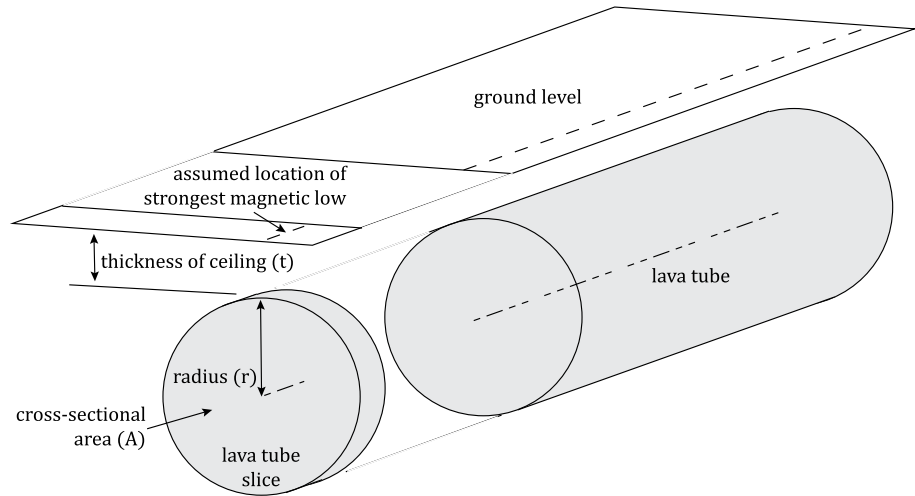


Figure 6. Schematic representation, of lava tube geometry deconstruction used for geomorphic versus geophysical relationship analysis between the lava tube geomorphology and the magnetic anomaly, used for this study.

5.1. Relating Magnetic Anomaly to Tube Geomorphology

In simplest terms, the magnetic signature of a lava tube is analogous to that of a buried cylindrical rod at depth, where the rod represents the void space of the lava tube. A negative linear relationship is expected between the magnetic anomaly and an increase in the geometric ratio of lava tube depth to cross-sectional area, with the slope being proportional to the susceptibility. If the lava tube anomaly provides a significant contribution above the background variation, this signal will be visible. The derivation for determining the total field magnetic anomaly ΔF , in nanotesla (nT); located directly above the longitudinal centerline of an infinite cylindrical magnet, with magnetic susceptibility k , equivalent radius r in meters, cross-sectional area A in meters squared, buried beneath a ceiling of thickness t in meters, with a depth to the center of the rod of $t + r$, where r is the radius of the cylinder in meters; shown in Figure 6, is given by Gay (1965) to be Equation 3:

$$\Delta F = \frac{k}{4\pi} \left(\frac{2T'_o \sin I_o \cos(2I'_o - 180^\circ)}{\sin I'_o} \right) \frac{A}{(t + r)^2} \quad (3)$$

where,

$$T'_o = \frac{T_o \sin I_o}{\sin I'_o} \quad (4)$$

and,

$$I'_o = \tan^{-1} \frac{\tan I_o}{\sin \alpha} \quad (5)$$

Here, T_o is the Earth's magnetic field in nT, I_o is the magnetic inclination, and α is the strike of the lava tube measured clockwise from magnetic north. For our purposes, the radius r , of the observed lava tubes, is defined to be an effective radius of the lava tubes based on the average of the height and width of the lava tube:

$$r = \frac{1}{2} \left(\frac{1}{2} \text{height} + \frac{1}{2} \text{width} \right) \quad (6)$$

We assume the magnetic inclination and strike of the lava tubes remain constant at 64.7° and $N90^\circ E$, respectively, for the LBNM location and approximate lava tube alignment for this study. With these values and setting the Earth's magnetic field equal to the average of the field on the days of the field surveys (50,613 nT), we define constant C_1 , which accounts for the geographic location and relative geometric position of the lava tube, to be:

$$C_1 = \left(\frac{2T'_o \sin I_o \cos(2I'_o - 180^\circ)}{\sin I'_o} \right) \quad (7)$$

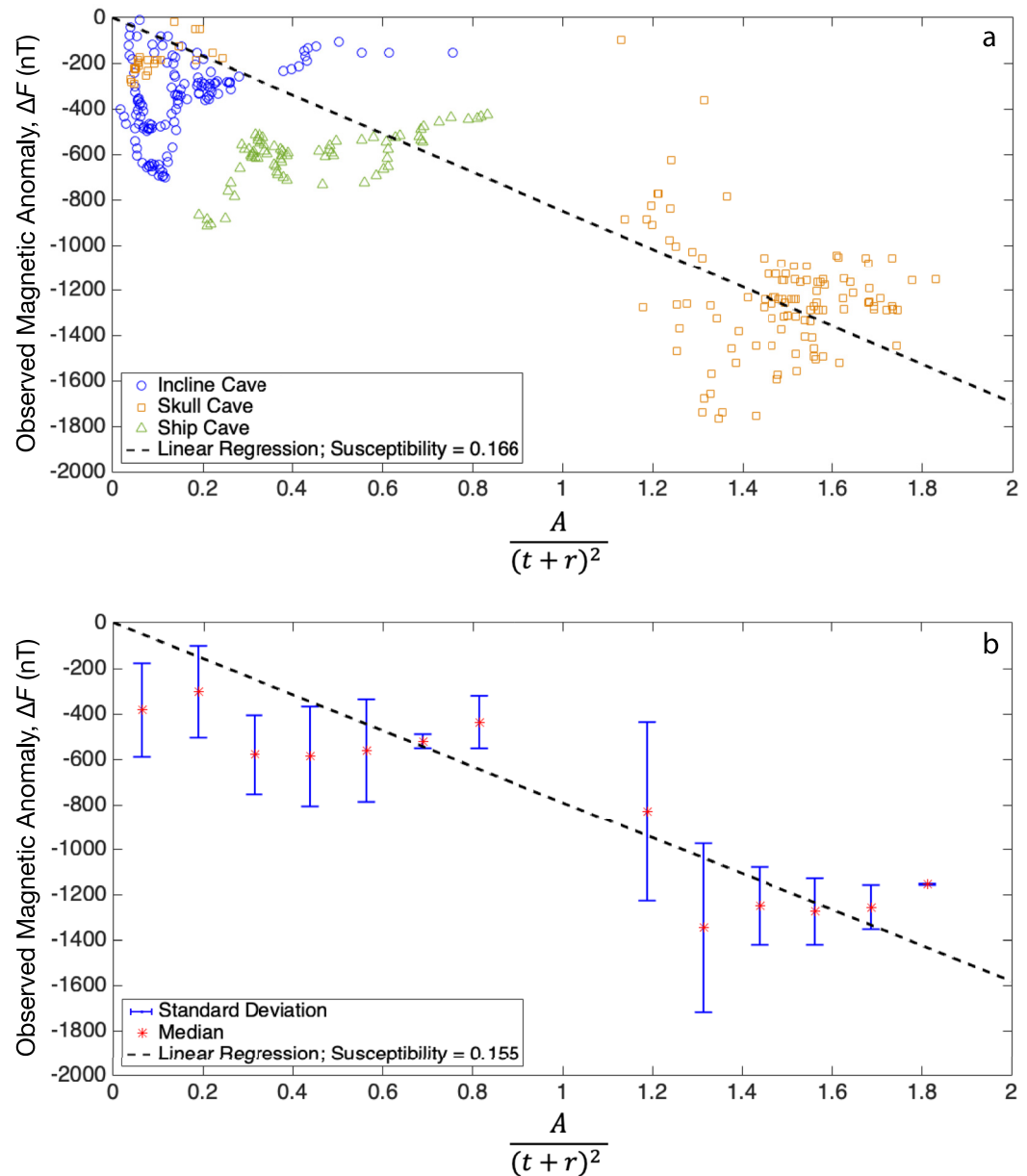


Figure 7. The relationship between the observed lava tube total field magnetic anomalies and the LiDAR-derived nondimensional geometric ratio. A linear least squares regression (broken black line) was used to determine the effective magnetic susceptibility. (a) All observed 1-m slice data points for Ship (green triangles), Incline (blue circles), and Skull (orange squares) caves. Effective magnetic susceptibility of 0.166 ± 0.007 . (b) Median of the observed data for every 0.125 geometric ratio increment. Error bars show one standard deviation from the median. Effective magnetic susceptibility of 0.155 ± 0.023 .

For our analysis, we divided each lava tube into 1-m cross-sectional slices along the west-to-east running longitudinal length. For each slice, across the regularly spaced lava tube point cloud models of the observed lava tubes, we determined the geometric ratio, defined as the cross-sectional area (A) over the square of the effective depth to the center ($t + r$) of the lava tube. For each of these cross-sectional slices, the strongest observed negative magnetic anomaly ΔF from the smoothed interpolated data, within the borders of the lava tube walls was determined. The minimum magnetic anomaly versus the geometric ratio of the observed data was then plotted for all three Modoc Crater lava tube system segments studied; Incline, Skull, and Ship Caves; and can be seen in Figure 7a. The scatter seen in Figure 7a is likely due to the interactions from the variations in the actual magnetic

properties and lava tube geometry along the longitudinal axis of the model. These data were then binned at 0.125 increments of the geometric ratio, along the X -axis, with the median for each of these bin groupings plotted in Figure 7b along with the one standard deviation error from the median for each bin. For these scatter plots, the best fit least squares linear regression line with a zero intercept was determined. As would be predicted by Equation 3 for a void within a lava flow, we observe an overall negative linear relationship between the strongest observed negative magnetic anomaly and an increase in the geometric ratio of lava tube depth to cross-sectional area. This suggests that it is probable that the tube anomaly is contributing to the variation we observed at the study region.

The slope of this linear relationship is related to the effective magnetic susceptibility for the family of lava tubes in the Modoc Crater lava tube system. Effective magnetic susceptibility is defined in this sense as the combination of the unknown true susceptibility and unidentified thermo-remanent magnetization into a single effective susceptibility parameter. For this calculation, we set the magnetic susceptibility (k) and the constant $\left(\frac{C_1}{4\pi}\right)$ equal to the slope of the plotted data and solve for the effective magnetic susceptibility (k) as follows:

$$k = \frac{4\pi}{C_1} \frac{\delta(\Delta F)}{\delta\left(\frac{A}{(r+r')^2}\right)} \quad (8)$$

This analysis results in an effective magnetic susceptibility of 0.166 ± 0.007 for the scatter plot of all data points in Figure 7a. Using the median data, Figure 7b, we calculate an effective magnetic susceptibility of 0.155 ± 0.023 . The calculated effective magnetic susceptibility is well with the range of measured susceptibilities for basaltic lava flows that can range of up to 0.4 S.I (Budetta & Negro, 1995). The recovered effective susceptibility of 0.155 was used for all our forward models.

5.2. Validation of Magnetic Anomaly to Geomorphic Relationship

Forward magnetic anomaly models that used the three-dimensional LiDAR point cloud representations of Incline, Skull, and Ship lava tubes allowed us to test the sensitivity of our magnetic anomaly to geomorphic relationship using the assumption of a known effective magnetic susceptibility for the region. If effective magnetic susceptibility of the lava and the spatial variation in the total field magnetic anomaly are known, then the result shows that a suspected underlying lava tube geometry can be bounded, and subsurface cavity space inferred.

Per our assumption of relating the full magnetic anomaly to an effective induced magnetism, we set the remanent magnetism to zero. We then perform the modeling based purely on an effective magnetic susceptibility value of 0.155 ± 0.023 determined from observed geometric ratio versus magnetic strength analysis. The resulting two-dimensional aerial magnetic anomaly maps are shown in Figures 4g–4i. The same geomorphic analysis performed on the observed data (results in Figure 7) was repeated on the results of our modeled lava tube magnetic signatures, with plots of this analysis shown in Figure 8. The scatter seen in Figure 8a is due to the effects of the variations in the actual geometry of the lava tubes and overburden thickness along the longitudinal axis of the model. These model results show good agreement to the observed data analysis, returning an effective magnetic susceptibility of 0.168 ± 0.014 , Figure 8b, versus 0.155 ± 0.023 , which is a difference of 8%, with overlapping error margins. This difference is likely a combination in the differences between true geometries and the simple cylindrical model, as well as unaccountable variations in magnetization in the actual lava flow itself. This demonstrates that the magnetic anomalies of natural lava tube systems, such as those studied here, can be approximated by a cylindrical theoretical model as long as the observed magnetic signal of the lava tube itself is greater than the background variation.

The practical capability acquired from this magnetic to geometric relationship for lava tubes is to use magnetic anomalies to help estimate the possible geometric ratio of lava tubes. This can be done with the addition of one independently acquired geometric constraint on a lava tube (depth to ceiling), along with the local magnetic properties (i.e., effective susceptibility or remanent magnetization) of the lava, it is possible to constrain the range of lava tube cross-sectional geometries based on a surface map of the magnetic anomaly created by a lava tube with sufficient signal to background variation. For example, by using field susceptibility measurements to determine the correct susceptibility curve, along with the magnetic anomaly strength from a field survey, the geometric ratio can be determined. Then, by using the depth to lava tube ceiling, or in other words the overburden thickness,

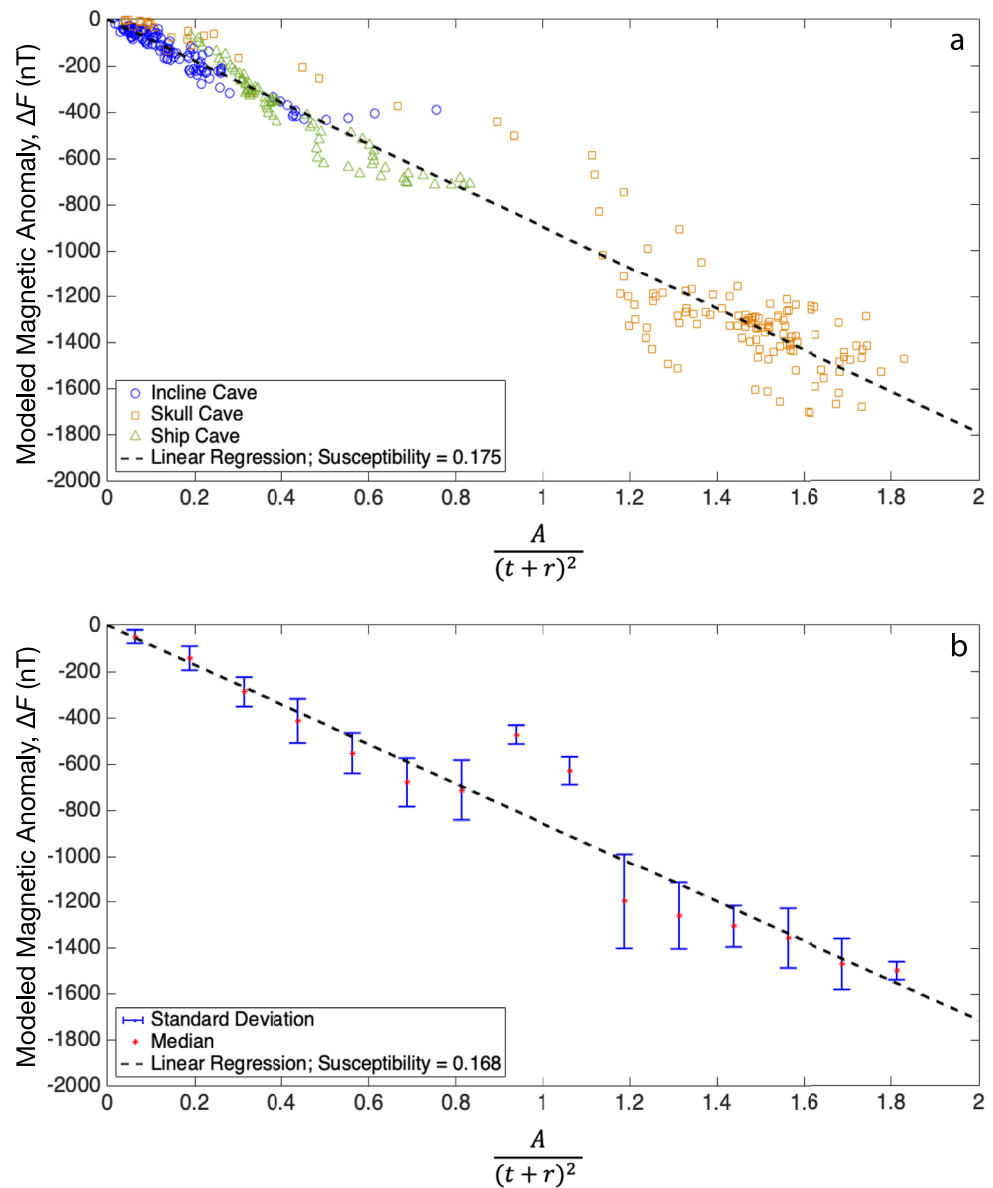


Figure 8. The relationship between the modeled lava tube total field magnetic anomalies and the LiDAR-derived nondimensionalized geometric ratio. A linear least squares regression (broken black line) was used to determine the effective magnetic susceptibility. (a) All modeled 1-m slice data points for Ship (green triangles), Incline (blue circles), and Skull (orange squares) caves. Effective magnetic susceptibility of 0.175 ± 0.002 . (b) Median of the modeled data for every 0.125 geometric ratio increment. Error bars show one standard deviation from the median. Effective magnetic susceptibility of 0.168 ± 0.014 .

which can be acquired either from visual inspection of a lava tube at a collapsed pit, or via other geophysical field methods such as ground penetrating radar (Esmaeili et al., 2020; Miyamoto et al., 2005) the effective cross-sectional radius for a lava tube can be calculated.

To demonstrate calculating an effective lava tube radius we used data from Incline, Skull, and Ship Caves. This process is tabulated in Table 2 and all row numbers referenced in this section are Table 2 entries. We used the medians of the strongest negative magnetic anomalies, ΔF , and the tube overburden thickness, t , based on all perpendicular slices used in the geomorphic to magnetic analysis (Rows 1 and 5). Along with this data, we used the effective magnetic susceptibility of 0.155, which we calculated for our field section of the Modoc Crater lava tube complex. Then rearranging Equation 3, we solve for the effective lava tube radius, r (Row 9), that would be

Table 2

For Incline, Skull, and Ship Lava Tube Caves the Following Values Are Provided Based on Calculated and Observed Data

		Incline cave	Skull cave	Ship cave
1	Observed Median Max Negative Magnetic Anomaly (nT)	−345	−1,177	−605
2	Observed Mean Magnetic Anomaly Within Tube Perimeter (nT) (\pm signal variation)	-161 ± 306	$-29 \pm 1,095$	-364 ± 287
3	Overall Tube Area (nT) (\pm background variation)	44 ± 421	92 ± 784	-250 ± 282
4	Signal Variation to Background Variation	0.73	1.40	1.02
5	Observed Median Overburden Thickness (t) (m)	12.60	4.2	10.2
6	Observed Median $\frac{1}{2}$ Width (m)	5.5	10.6	8.8
7	Observed Median $\frac{1}{2}$ Height (m)	2.3	7.5	4.1
8	Effective Radius (r) Observed Median (m)	3.9	9.1	6.4
9	Calculated from Magnetic Anomaly (m)	7.5	9.3	9.9
10	Error Ratio: Observed/Calculated	0.52	0.98	0.65
11	Ratio: Observed Effective Radius (r)/Overburden (t)	0.31	2.17	0.63

Note. (1) The observed median of the maximum negative magnetic anomaly over the lava tube. (2–4) The observed mean magnetic anomaly from: (2) within the tube perimeter, (3) the overall region of observation over the lava tube, and (4) the ratio of the signal variation (in row 2) to background variation (in row 3). (5) The observed median overburden thickness for the lava tube. (6) The observed median $\frac{1}{2}$ width for the lava tube. (7) The observed median $\frac{1}{2}$ height for the lava tube. (8–10) The effective radius (r) for: (8) the actual observed median effective radius, (9) the calculated effective radius based on the median maximum negative magnetic anomaly and the median observed overburden thickness, and (10) the error ratio of the two (8–9). (11) The ratio of the observed effective radius (8) to overburden (5).

required to create the median strongest negative magnetic anomaly. Row 10 then provides the ratio of observed median (Row 8) to this calculated effective radius (Row 9), with 1 being an exact fit and values less than 1 corresponding to an overestimation of effective tube radius.

The results of this example for a first order approximation of the effective radius of the three lava tubes provide an insight into trends to guide continued research in this area. The first of these trends is a comparison of the signal to background variation between Incline, to Ship, and Skull caves. For this comparison, we first calculated the means and standard deviations from the observed data for the field site above and extending to the approximately two to three widths to each side of the lava tube, as available from the area survey, to represent normal variation in the magnetic signal in the site location, defined as background variation (Row 3). The signal from the tube itself was included in the background variation to provide the analog situation for surveying an area with unknown tube locations. We then assumed the ground level area outlined by the extents of the lava tube to represent the magnetic signature presented from the lava tube itself, defined as the signal (Row 2). The resulting signal to background variation ratio is provided in Row 4, showing an increase from Incline, to Ship, to Skull caves. We can then see that there are similar trends from Incline, to Ship, to Skull caves for overburden thickness (Row 5), the observed median effective radius (Row 8), and the resulting ratio of effective radius to overburden (Row 11). These match the trend between the caves for the results of the error ratio of observed to calculated effective radius, shown in Row 10, where a result of 1 would be an exact fit of the calculated lava tube effective radius compared to the observed median. This quantifies the understanding of the importance of the relative nature between tube size and depth in relation to background variation. This can be generalized as: small deep lava tubes are difficult to resolve, whereas large shallow tubes have ideal signal to background variation and geometric ratios for locating.

It is likely that the tube signal and background variation are both partially dependent on the formation process and evolution of lava flows in the area which likely introduces background variation into the system that is not explicitly addressed in this research. For instance, a lava tube formation mechanism of either coalescing of previously solidified rafted plates, already cooled below the Curie point, may result in a final lava tube roof constructed of essentially individually remanently magnetized plates with random orientations resulting in a lack of a uniform magnetic background signature. This would add variation on the scale of meters to tens of meters on top of the tube's magnetic signature which may then lie below this variation. Similarly, the lava tube formation processes by construction of arches from border levees along turbulent flow can be envisioned to result in individual spatter components cooling below the Curie point, and then having a physical change in orientation due to the addition of additional spatter as the arch is created. Pahoe and stable channel flow surface solidification processes can be envisioned to result in less physical orientation rearrangement after a remanent magnetic set as it cools

below the Curie point, thus these would be expected to have relatively large spatial coherency. However, even these formation processes can have changes in positioning as they cool due to changes in channel flow depth, or inflation/deflation of pahoehoe lobes, which could still result in adding to the complexity of the magnetic background variation, albeit less than from construction transport processes. Follow-on flows after the original construction of a lava tube could be envisioned to impact the magnetic signature as they potentially alter the location of previously emplaced basalt, or increase the ceiling thickness with randomly oriented blocks of a'a basalt on the scale of size of the magnetic measurements. Finally, the impact of the roughness (or blockiness) of the lava flow, along with possible unknown and therefore unaccounted for void spaces in the lava tube ceilings during the formation evolution can result in increased complexity in the magnetic background variation. This complexity will interact in a nonuniform fashion which increases the magnetic background variation. These impacts to the magnetic background variation would be more pronounced in lava tubes with smaller effective radius to depth ratios such as Incline and Ship Caves, and these details are not accounted for in the resolution used for constructing these models.

Overall, these trends show that the Skull Cave segment produces magnetic anomalies of significant magnitude above the background variation that allow us to reliably determine the overall radius of the lava tube. This signal to background variation for Skull Cave is likely amplified primarily because the ratio of radius to ceiling depth for Skull Cave is three to seven times larger than for Incline and Ship Caves. This higher ratio at Skull Cave results in the tube producing a magnetic anomaly that is not lost in the magnetic background variation from the lava flow and lava tube formation processes.

5.3. Interpretation and Utility of Magnetic Gradient Analysis

As described in Sections 3.3 and 4.2, the two-dimensional gradients of the ground level magnetic signatures for the three lava tubes were also investigated and are shown in Figure 5. For each of the model results (Figures 5d–5f), this analysis shows well-defined lines of minimal gradients that track the outlines of the lava tube perimeter, with a slight offset to the north, likely due to the magnetic inclination at LBNM of 64.7°.

Conversely, for the observed magnetic gradients at Incline and Ship Caves (Figures 5a and 5c), there is very little to no area in which gradient lines are associated with the location of the actual lava tubes. This is again likely due to the ratio of the effective radius to depth for these caves being too low for the magnetic signature of the cave to overcome the magnetic background variation. As previously discussed, the background variation is possibly due to items such as small-scale perturbations in the magnetic fields from random orientations of basaltic blocks and small void spaces in the lava tube ceiling, or from other sources such additional lava flows, all interacting in a nonuniform fashion, and overriding the magnetic gradient created from the perimeter of the lava tubes.

However, Skull Cave, with the highest effective radius to overburden ratio of this study, has magnetic gradients (Figure 5b) that exhibit three distinct curvilinear minima. The southern two of these lines align with the locations of the actual Skull Cave walls, similar to the modeled results. There is a slight variation of the northern of these two lines (center line of the three) aligning perfectly with the northern wall of Skull Cave versus being slightly offset to the north as seen in the results from the modeled data (Figure 5e). This position of the center line of minimal magnetic gradient may be affected by a second significant negative magnetic anomaly parallel and to the north of the one overlapping Skull Cave. This additional negative magnetic anomaly may be affecting the positive magnetic anomaly from Skull Cave, moving it slightly to the south, which would account for this variation. The third line, furthest north, of minimal magnetic gradient in the observed Skull Cave data analysis is also due to this second negative magnetic anomaly, which is produced by a currently unknown source.

One item of note from the results of Skull Cave is that these magnetic gradient lines have the potential to be used for an initial estimate of the width of the lava tube. For example, the width based on the observed magnetic gradient plot can be estimated to be approximately 20 m across, which is similar to the true median observed width of 21.2 m (based on Table 2, row 7). We can then apply the half-width of 10 m along with the calculated effective radius of 9.3 m (Table 2, row 9) to Equation 6 to calculate a half-height of 8.6 m. The observed median half-height is 7.5 m, or a difference of 13%.

5.4. Comparisons of Lava Tube Magnetic Surveys and Models

When comparing the observed and modeled magnetic survey maps there are similarities as well as some variations between the two sets. This can be noticed by comparing the magnetic anomaly maps in Figure 4, as well as comparing the data points in the scatter plots of the magnetic anomalies versus tube geomorphology seen in Figures 7 and 8. For Incline Cave, the observed magnetic anomaly has a similar functional form to the modeled anomaly in the western half of the tube (Figures 4d and 4g). Despite these similarities, the modeled magnetic low for the remainder of the tube is approximately equal to or less than the background variation of the observed data (approximately -400 nT, see Table 2). In this same area (the eastern half), the ratio of the effective tube radius to overburden thickness significantly decreases providing an explanation for the lack of observed magnetic signature of eastern Incline Cave.

There is a similar effect seen in the comparison for Ship Cave (Figures 4f and 4i), although the tube has a signal to background variation of ~ 1.0 . Specifically, the expected positive magnetic anomaly associated with the lava tube is present on the north side of the tube for both the observed and modeled data, albeit of a higher magnitude and further north in the observed data. Also, the observed data shows some negative anomalies over the tube location that are slightly above the background magnetic variability similar to the model, which suggests that the signal to background variation of the tube versus the background is somewhat variable (i.e., there are a few places where the signal is noticeable above the background variation).

Skull Cave (Figures 4e and 4h) provides the most pronounced magnetic signature and best agreement between the observed and modeled magnetic maps. At Skull Cave, two approximately $-1,500$ nT east-west parallel magnetically low anomalies flank an approximately $+1,500$ nT anomaly, as seen in Figure 4e. The southern of these two negative anomalies, lying over the location of Skull Cave, matches very well with the strength of the modeled negative anomaly for this lava tube. The location of the observed positive anomaly also matches the location of a positive anomaly in the model, though the observed peak is four times the expected magnitude from modeling. The other primary difference between the observed and modeled magnetic maps is the strong northern negative magnetic anomaly, which does not exist in the model results, but is the reason for additional lines of minimal magnetic gradient (Figure 5b) as discussed earlier. This raises the question as to the origin of the northerly located negative magnetic anomaly.

5.5. Magnetic Fields Identify Unknown Candidate Tubes

As can be seen on Figure 3, known intact lava tubes align with recorded magnetic lows. In addition, there is a magnetic low that appears to originate from an unmapped tube location north of Skull Cave. However, it is unconfirmed if a void space exists at this position due to a lack of accessibility into the area. This region of interest is labeled as “suspected subsurface void.”

In Figures 2 and 3, it can clearly be seen that there is a collapsed pit just to the east of Skull Cave that is more than twice the width of Skull Cave and the other collapsed pits in this tube complex. This gives rise to the hypothesis that this location contained either a lava tube wider than the Skull Cave segment, or a parallel bifurcated section of the Modoc Crater lava tube system. If there were parallel lava tubes at the collapsed pit location, the northerly negative anomaly seen near Skull Cave may be the magnetic signature of an inaccessible portion of the remnants of a second lava tube of similar scale as Skull Cave.

To address this question, a simple model was created of two parallel lava tubes with surrounding magnetic susceptibility of 0.155. For this model, we duplicated the Skull Cave LiDAR survey to the north of its true location, at an offset of 40 m from the southern wall. This geometry separates the twin lava tubes with a wall thickness varying between approximately 15–20 m. The results (Figure 9a) show a slight magnetic high between the twin lava tubes, with a negative magnetic anomaly above each tube. Additionally, there is a stronger positive magnetic anomaly north of both lava tubes. The resulting magnetic gradient for this twin model, presented in Figure 9b, shows four distinct lines of minimal magnetic gradient, of which the southern three are similar to the three lines of minimal slope seen in the observed magnetic gradient in Figure 5b. Although not an exact match of the magnetic signature seen at Skull Cave, there are significant similarities, with the model's primary difference being the low amplitude of the positive magnetic anomaly between the two negative anomalies.

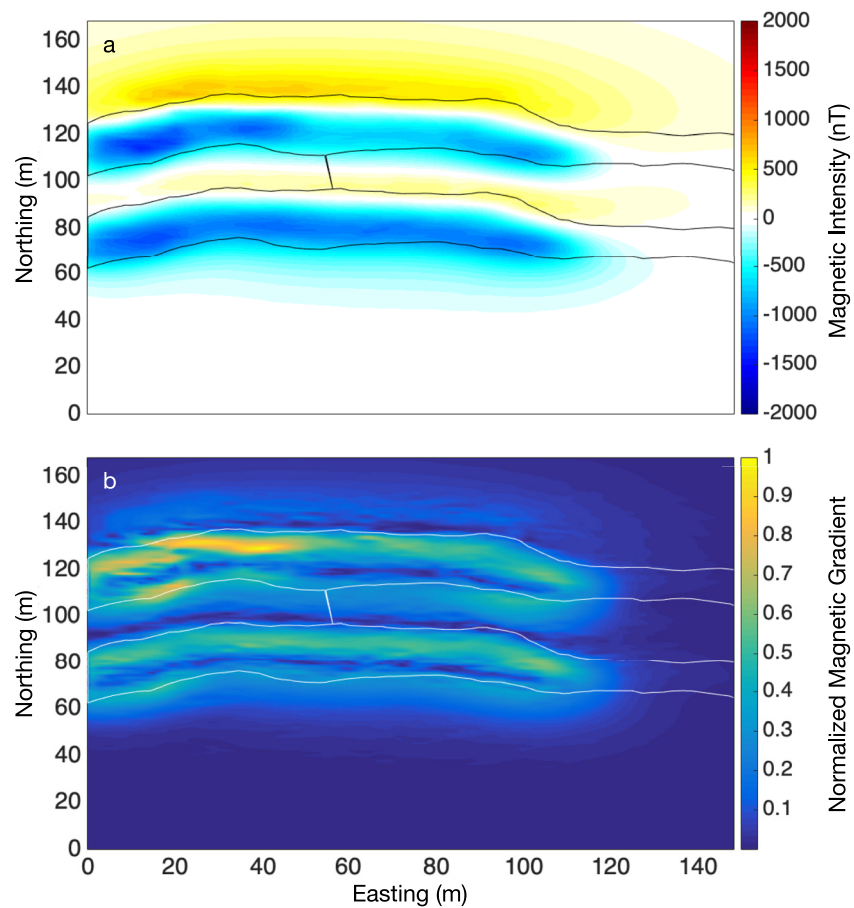


Figure 9. Magnetic anomalies and gradients for theoretical double tube models at Skull Cave location. (a) Plot of magnetic anomalies from application of magnetic susceptibility of 0.155. (b) Magnetic gradient plot normalized to the highest gradient (nT/m) calculated.

It is understood that magnetic modeling is a nonunique technique to analyze a potential field, and thus we cannot confirm, completely independent of other geophysical methods, the existence of a previously unknown, and inaccessible parallel tube of similar size to Skull Cave. However, the negative magnetic anomaly north of Skull Cave coupled with the strong positive anomaly would suggest a complex history of formation at this location. This history may include a bifurcating branch parallel to Skull Cave, or additional thermal-magnetic or thermal-chemical alterations to this segment of the Modoc Lava Tube System, which might have increased the effective magnetic susceptibility of the tube wall to the north of Skull Cave (Garrick-Bethell & Weiss, 2010; Hemingway & Tikoo, 2018; Xu et al., 1997).

Future observations of this field site using additional geophysical techniques are warranted to aid in increasing the understanding of the formations in place. These analyses when combined with similar observations from other field sites have the potential to offer a new understanding into the lava flow processes and the extent to which lava tubes, and voids, exist within a lava flow.

5.6. Implications for Lunar Lava Tubes

There are several differences between lava tubes on the Moon and the terrestrial tubes in this study. For instance, the magnetic properties of the regolith covering the lunar surface are unknown at high spatial resolution (sub-10 m), so the magnetic background variation found on the Moon's surface will need to be assessed at target study locations on the Moon. Also, variations in strength, orientation, and complexity of the lunar dynamo throughout lunar history may have influenced remanent magnetic signatures preserved at tube-hosting lava flows. Finally, the lack of a current lunar dipole magnetic field versus the ~50,000 nT Earth dipole results in a reliance on

observations of these purely remanent magnetic signatures from the lunar surface to conduct analysis, versus this Earth-based analysis which assumes an effective induced magnetism.

Despite these differences, it is expected that the remanent magnetic signature of lunar lava flows can provide sufficient anomalies to detect candidate locations to search for lava tubes, as well as bound their internal geomorphology. For surveys conducted on the lunar surface, within 2 m of the ground, magnetic anomalies are known to range from 5 to 313 nT from Apollo mission stationary and portable magnetometer observations, and surface-level anomalies are estimated to be >500 nT, in select regions, from Kaguya and Lunar Prospector observations (Dyal & Gordon, 1973; Tsunakawa et al., 2015). Assuming a lunar lava tube magnetic anomaly is of the same relative order of magnitude with respect to the background variability as seen at Skull Cave (signal to background variation ~1.4), the resulting magnetic anomaly would be in the range of 10–100s of nT, which is well within the resolution capability of the current state of the art for spaceborne magnetometers (Connerney et al., 2015, 2017). The biggest lunar lava tubes are theorized to be significantly larger than their terrestrial counterparts, on the order of 100–1,000s of meters in diameter (Blair et al., 2017). Thus, even ceilings as thick as 100 m would produce a ratio of lava tube effective radius to ceiling thickness of one or greater, comparable to the 2.17 value for Skull Cave. The larger lunar dimensions will create lunar lava tube magnetic signatures with longer wavelengths relative to local background variability. Of the tubes studied here, Skull Cave, with its >1 ratio of effective radius to ceiling thickness, is the best terrestrial analog for comparison to lunar lava tubes. With the addition of knowledge of the background magnetic variability on the Moon, added to the understanding of the potential size and shape of lunar lava tubes, we can constrain the ability to detect the magnetic anomalies of lunar lava tube.

To develop lunar equivalent plots for magnetic anomaly verses lava tube geometric ratio as in Figures 7 and 8, we must convert the use of induced magnetism used in Equation 8, to using the remanent magnetic property of the lunar basalt. To do this, we begin with the equation of the total magnetic strength, j_T , being the summation of the induced magnetism, j_{oI} , and the remanent magnetism, j_{oR} , or

$$j_T = j_{oI} + j_{oR} \quad (9)$$

For the terrestrial analysis of LBNM, we assumed that the remanent magnetism portion was zero and calculated an effective magnetic susceptibility. This effective susceptibility accounted for both the induced as well as remanent portion, which cannot be separated without additional sample testing for the actual remanent magnetic properties of the basalt in the field site. Magnetic analysis is commonly combined in this fashion for terrestrial applications. In isolation, induced magnetic strength, j_{oI} , is related to the magnetic susceptibility, k , the intensity of the Earth's magnetic field at the location of interest in nT, T_o , and magnetic permeability, μ (Hinze et al., 2013):

$$j_{T,earth} \approx j_{oI} = \frac{k T_o 10^{-9}}{\mu} \quad (10)$$

where j_{oI} has units of A/m. We assume $\mu = \mu_0 = 4\pi \times 10^{-7}$, which is the magnetic permeability in a vacuum.

Using Equation 10, we can rewrite Equation 8 to relate the expected magnetic anomaly from a lava tube (ΔF) directly to its magnetic field strength, j_T , instead of to its relationship to an exogenous field via its parent rock's susceptibility:

$$\frac{\delta(\Delta F)}{\delta\left(\frac{A}{(t+r)^2}\right)} = \frac{j_T 2 \times 10^2 \sin^2 I_o \cos(2I'_o - 180^\circ)}{\sin^2 I'_o} \quad (11)$$

In Equation 11, I_o and I'_o continue to be the inclination and effective inclination of the magnetic field, respectively, whether produced from induced or remanent magnetization. Again, in the terrestrial analysis above, we assume the magnetic strength j_T of the basalts to effectively be sourced from an induced magnetic field. However, on the Moon anomalies in the absence of a lunar magnetic field will arise from remanently magnetized bodies (i.e., $j_T \approx j_{oR}$).

To calculate the expected anomaly magnitude of tubes on the Moon, we can examine the remanent magnetism of lunar samples and analogous terrestrial basalts and the modeled strengths from lunar magnetic anomalies. Using four example strengths and magnetic field orientation values from our terrestrial field site (field inclination: 64.7°; tube orientation to horizontal field component: 90°), we plot the expected lunar magnetic anomaly versus

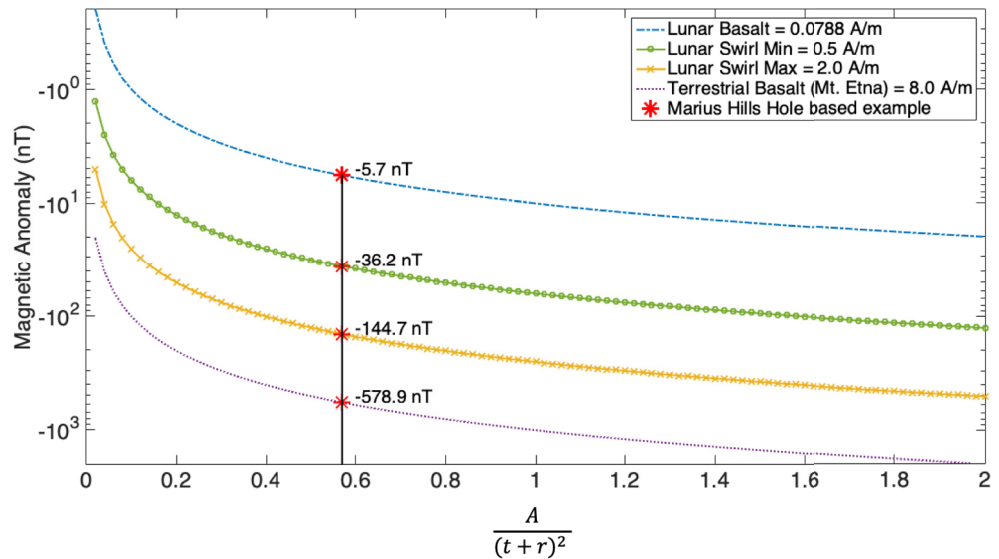


Figure 10. Plot of theoretical lava tube magnetic anomaly strength versus the geometric ratio for lava tubes based on remanent magnetic properties, simulating lunar equivalent lava tube signatures. The four lines represent: (a) the lowest anticipated remanent magnetic anomalies based on remanent strength of Apollo samples (dashed blue line); (b) lower bound for lunar swirl required magnetic strength (green circle line); (c) upper bound for lunar swirl required magnetic strength (yellow cross-hatched line); and (d) terrestrial equivalent remanent magnetic strength sampled from Mount Etna, Italy (purple dotted line). The Marius Hills example based on known ceiling thickness and depth to floor at the Marius Hills Hole, with assumed oval lava tube cross section with 2 to 1 ratio of width to height resulting in a geometric ratio of 0.57 is plotted crossing each of these lines at red asterisk.

lava tube geometric ratio, shown in Figure 10. We show lines for several assumed remanent magnetic strengths to attempt to bound the magnitude of the magnetic anomalies that may be observed on the lunar surface. The four curves represent different remanent magnetism (j_{or}) scenarios that might be present at lunar lava tubes. First, one curve employs a natural remanent magnetism of $2.51 \times 10^{-5} \text{ Am}^2 \text{ kg}^{-1}$, based on a study of the Apollo lunar basalt samples by Cournède et al. (2012), which equates to a remanent magnetic strength of 0.0788 A/m assuming a lunar basaltic density of $3,140 \text{ kg m}^{-3}$ (Kiefer et al., 2012). Two additional curves were derived using remanent magnetic strengths of 0.5 and 2.0 A/m, the minimum and maximum estimates of remanent magnetism required to produce lunar swirl complexes (Hemingway & Tikoo, 2018). The final curve was derived using a natural remanent magnetism of 8 A/m based on the mean remanent magnetization of the basaltic Etnean lava flows of 1910 and 1950 (Negro & Ferrucci, 1998).

From Figure 10 we estimate the potential strength of a magnetic anomaly produced by a theoretical lunar lava tube. For this example, we extend the known dimensions of the ceiling thickness and void height at the MHH collapsed pit (Figure 1c) into a lava tube of oval geometry with a width to height ratio of 2:1. Data from LRO shows the depth of this pit from the lunar surface is between 80 and 88 m, and has an original ceiling thickness of at least 40 m (Haruyama et al., 2009; Robinson et al., 2012; Wagner & Robinson, 2014). Assuming a ceiling overburden thickness, t , of 40 m, a lava tube height of 44 m (average depth minus overburden), and a width of 88 m (assuming 2-to-1 ratio of width to height) results in an effective radius (Equation 6) to ceiling thickness ratio of 0.75 and a geometric ratio of $\frac{A}{(t+r)^2} = 0.57$, which are between those for Ship and Skull caves in LBNM. Assuming this geometric ratio, from Figure 10 the resulting lunar magnetic anomaly would be approximately -5.7 nT in a low lunar remanent magnetism region, from -36 to -145 nT in a lunar swirl area, or as high as -579 nT in a region with remanent magnetism similar to terrestrial basalt. The minimum 5.7 nT anomaly is two orders of magnitude greater than the digital resolution of current spaceborne magnetometers (Connerney et al., 2015, 2017). Determining the regional magnetic background variability, as well as sources for the variabilities will be a key factor in the application of this technique on the Moon and other planetary locations. If magnetic background variability is less than the strength of the lava tube anomaly, the results can be applied to estimate the actual geometry of a lunar lava tube.

6. Conclusions

We have shown that where the magnetic anomaly produced by a lava tube is above the magnetic background variation, the maximum negative magnetic anomaly produced by a lava tube follows the magnetic signature predicted for a simple cylindrical void embedded in media with uniform magnetic susceptibility. With this model the magnetic minimum can be related to a nondimensional geometric ratio that is based on the depth and cross-sectional dimensions of the lava tube. This model was validated using three-dimensional LiDAR maps of lava tubes in LBNM. For LBNM, these magnetic anomalies become easily observable for lava tubes such as Skull Cave, with a geometric ratio >1 and a median signal to background variation of 1.4. Importantly, lava tubes which formed at non-perpendicular orientations with respect to the global magnetic field or at epochs where the magnetic field was reversed would exhibit magnetic anomalies with different geometries, which would require a modification to the model presented in this study.

The magnetic gradients produced at lava tubes in a high magnetic signal to background variation environment are shown to reveal the perimeter of lava tubes with large magnetic gradients, as seen at Skull Cave in LBNM. Use of this gradient analysis can constrain the width of a lava tube and, when coupled with the geometric ratio from the anomaly analysis, further constrain the dimensions of a lava tube. The gradient analysis may also be used to illuminate undiscovered lava tubes.

Finally, even with the lack of a current lunar dipole field, residual remanent magnetism could provide a way to detect lava tubes on the Moon. The magnetic anomaly to geometric ratio model can be generalized to the Moon to predict the magnetic anomaly of a lunar lava tube, provided independent constraints on the geometry such as ceiling thickness and magnetic properties. These methods have the potential to aid in the prospecting and evaluation of lunar lava tubes for the most desirable targets to continue additional robotic or human scientific investigation or for human utilization.

Acknowledgments

This work was performed in coordination with the NASA TubeX team whose research investigating field technologies and strategies for lava tube exploration is supported by NASA PSTAR grant NNX16AK11G and the Goddard Instrument Field Team. Support was provided by the NASA PSTAR grant NNX15AL87G supporting geophysical analog studies. Work by E. Bell, P. Whelley, and J. Richardson was supported by NASA under award #80GSFC17M0002. Additional funding for this project was supported by the NASA SSERVI GEODES Grant 80NSSC19M0216; This study was granted access to Lava Beds National Monument per U.S. Department of Interior National Park Service, Scientific Research and Collecting Permit, Study #LBE-00070, Permit #2017-LBE-SCI-0005. Caves observed in this study are designated 4-letter cave identification codes by the Lava Beds National Monument in addition to their names. These include M340 (Incline Cave), M350 (Skull Cave), and M380 (Ship Cave). The authors would also like to thank the staff and park rangers, including Randall Paylor and Katrina Smith, of LBNM, CA, USA for their support, expertise, and providing guidance and access to the lava tubes studied. Additionally, the authors would like to acknowledge the invaluable support and advice provided by the colleagues of the NASA Goddard Volcanology Writing Group. Finally, the authors would like to thank the reviewers who provided valuable suggestions to clarify details within the manuscript.

Data Availability Statement

The total magnetic field and LiDAR point cloud data used for the analysis and modeling in this study are available at the University of Maryland, University Libraries, Digital Repository at the University of Maryland (DRUM) online data repository. Within DRUM, the data files are located in the College of Computer, Mathematical & Natural Sciences department community; Geology sub-community; GEODES Data collection located at <http://hdl.handle.net/1903/26667>, with the title of LiDAR and Magnetic Data for: Field Mapping and Modeling of Terrestrial Lava Tube Magnetic Anomalies as an Analog for Lunar Lava Tube Exploration and Prospecting and a DOI of <https://doi.org/10.13016/ovqx-j09w>. For the purpose of review, these data files have been temporarily uploaded to the Supporting Information of the submission system for access by reviewers and editors.

References

- Arnold, C. (1986). *Inside the caves*. Charles L. Arnold.
- Bell, E., Schmerr, N., Young, K., Bleacher, J., Esmaeili, S., Garry, W. B., et al. (2020). *Magnetic signatures OF terrestrial lava tubes as analogs for lunar* (p. 2294). Retrieved from <https://www.hou.usra.edu/meetings/lpsc2020/pdf/2294.pdf>
- Bell, E., Schmerr, N., Young, K., Whelley, P., Garry, W. B., Kruse, S., et al. (2018). *Characterization OF lava tubes with magnetometry* (p. 2412). Retrieved from <https://www.hou.usra.edu/meetings/lpsc2018/pdf/2412.pdf>
- Binder, A. B. (1998). Lunar prospector: Overview. *Science*, 281(5382), 1475–1476. <https://doi.org/10.1126/science.281.5382.1475>
- Blair, D. M., Chappaz, L., Sood, R., Milbury, C., Bobet, A., Melosh, H. J., et al. (2017). The structural stability of lunar lava tubes. *Icarus*, 282, 47–55. <https://doi.org/10.1016/j.icarus.2016.10.008>
- Bleacher, J. E., Orr, T. R., de Wet, A. P., Zimbelman, J. R., Hamilton, C. W., Brent Garry, W., et al. (2017). Plateaus and sinuous ridges as the fingerprints of lava flow inflation in the Eastern Tharsis Plains of Mars. *Journal of Volcanology and Geothermal Research*, 342, 29–46. <https://doi.org/10.1016/j.jvolgeores.2017.03.025>
- Bongiolo, A. D. B. E. S., Souza, J. D., Ferreira, F. J. F., & Castro, L. G. D. (2013). Grav_mag_prism: A MATLAB®/octave program to generate gravity and magnetic anomalies due to rectangular prismatic bodies. *Revista Brasileira de Geofísica*, 31(3), 347–363. <https://doi.org/10.22564/rbfg.v31i3.310>
- Budetta, G., & Negro, C. D. (1995). Magnetic field changes on lava flow to detect lava tubes. *Journal of Volcanology and Geothermal Research*, 65(3–4), 237–248. [https://doi.org/10.1016/0377-0273\(94\)00108-S](https://doi.org/10.1016/0377-0273(94)00108-S)
- Burger, H., Sheehan, A., & Jones, C. H. (2006). *Introduction to applied geophysics: Exploring the shallow subsurface* (Vol. 550). WW Norton.
- Calvari, S., & Pinkerton, H. (1998). Formation of lava tubes and extensive flow field during the 1991–1993 eruption of Mount Etna. *Journal of Geophysical Research*, 103(B11), 27291–27301. <https://doi.org/10.1029/97JB03388>
- Chappaz, L., Sood, R., Melosh, H. J., Howell, K. C., Blair, D. M., Milbury, C., & Zuber, M. T. (2017). Evidence of large empty lava tubes on the Moon using GRAIL gravity. *Geophysical Research Letters*, 44(1), 105–112. <https://doi.org/10.1002/2016GL071588>

- Connerney, J. E. P., Benn, M., Bjarno, J. B., Denver, T., Espley, J., Jorgensen, J. L., et al. (2017). The Juno magnetic field investigation. *Space Science Reviews*, 213(1–4), 39–138. <https://doi.org/10.1007/s11214-017-0334-z>
- Connerney, J. E. P., Espley, J., Lawton, P., Murphy, S., Odom, J., Oliverson, R., & Sheppard, D. (2015). The MAVEN magnetic field investigation. *Space Science Reviews*, 195(1–4), 257–291. <https://doi.org/10.1007/s11214-015-0169-4>
- Cournède, C., Gattacceca, J., & Rochette, P. (2012). Magnetic study of large Apollo samples: Possible evidence for an ancient centered dipolar field on the Moon. *Earth and Planetary Science Letters*, 331–332, 31–42. <https://doi.org/10.1016/j.epsl.2012.03.004>
- Crown, D. A., Berman, D. C., Scheidt, S. P., & Hauber, E. (2019). Geology of Alba Mons, Mars: Results from 1: 1M-scale geologic mapping. In A. David (Ed.), *Lunar and Planetary Science Conference* (Vol. 2).
- Cushing, G. E., Titus, T. N., Wynne, J. J., & Christensen, P. R. (2007). THEMIS observes possible cave skylights on Mars. *Geophysical Research Letters*, 34(17), L17201. <https://doi.org/10.1029/2007GL030709>
- DeDecker, J. (2014). *Evaluation of lava tube formation mechanisms using three-dimensional mapping and viscosity modeling: Lava Beds National Monument, California* (Master of Science). University of North Carolina.
- Doell, R. R., Grommé, C. S., Thorpe, A. N., & Senftle, F. E. (1970). Magnetic studies of lunar samples. *Science*, 167(3918), 695–697. <https://doi.org/10.1126/science.167.3918.695>
- Dolginov, S., Eroshenko, E. G., Zhuzgov, L. N., & Pushkov, N. V. (1966). Measurements of the magnetic field in the vicinity of the Moon by the artificial satellite Luna-10. *Kodlady, Akademii Nauk USSR*, 170, 574–577.
- Dolginov, S. S., Yeroshenko, E. G., Zhuzgov, L. N., & Pushkov, N. V. (1963). Investigation of the magnetic field of the Moon. *AIAA Journal*, 1(2), 514–516. <https://doi.org/10.2514/3.1589>
- Donnelly-Nolan, J. (2010). *Geologic map of Medicine Lake volcano, northern California* (Scientific Investigations Map No. Scientific Investigations Map 2927). U.S. Department of the Interior, U.S. Geological Survey.
- Duda, R. O., Hart, P. E., & Stork, D. G. (1973). *Pattern classification and scene analysis: Part I pattern classification*. John Wiley & Sons, Inc.
- Dyal, P., & Gordon, D. (1973). Lunar surface magnetometers. *IEEE Transactions on Magnetism*, 9(3), 226–231. <https://doi.org/10.1109/TMAG.1973.1067650>
- Esmaeili, S., Kruse, S., Jazayeri, S., Whelley, P., Bell, E., Richardson, J., et al. (2020). Resolution of lava tubes with ground penetrating radar: The TubeX project. *Journal of Geophysical Research: Planets*, 125(5), e2019JE006138. <https://doi.org/10.1029/2019JE006138>
- Ferreira, F. J. F., de Souza, J., Bongiolo, A. D. B. E. S., & de Castro, L. G. (2013). Enhancement of the total horizontal gradient of magnetic anomalies using the tilt angle. *Geophysics*, 78(3), J33–J41. <https://doi.org/10.1190/geo2011-0441.1>
- Frankel, C. (1996). *Volcanoes of the Solar System*. Cambridge University Press.
- Garrick-Bethell, L., & Weiss, B. P. (2010). Kamacite blocking temperatures and applications to lunar magnetism. *Earth and Planetary Science Letters*, 294(1–2), 1–7. <https://doi.org/10.1016/j.epsl.2010.02.013>
- Garry, W. B., Whelley, P., Shiro, B., Rowland, S., & Bleacher, J. (2017). *Analysis of a lava tube with Lidar on Mauna Loa volcano, Hawai'i* (Paper No. 25-3). Retrieved from <https://gsa.confex.com/gsa/2017CD/webprogram/Paper292954.html>
- Gay, S. P. (1965). Standard curves for magnetic anomalies over long horizontal cylinders. *Geophysics*, 30(5), 818–828. <https://doi.org/10.1190/1.1439656>
- GEM Systems, Inc. (2008). *GEM GSM-19 v7.0 instruction manual*. Retrieved from https://userpage.fu-berlin.de/geodyn/instruments/Manual_GEM_GSM-19.pdf
- George, O., McIlrath, J., Farrell, A., Gallant, E., Tavarez, S., Marshall, A., et al. (2014). High-resolution ground-based magnetic survey of a buried volcano: Anomaly B, Amargosa Desert, NV. *Statistics in Volcanology*, 1, 1–23. <https://doi.org/10.5038/2163-338X.1.3>
- Girardeau-Montaut, D. (2016). CloudCompare. Presented at the France: EDF R&D telecom. Paris Tech. Retrieved from http://pcp2019.ifp.uni-stuttgart.de/presentations/04-CloudCompare_PCP_2019_public.pdf
- Greeley, R. (1971a). Lava tubes and channels in the lunar Marius Hills. *The Moon*, 3(3), 289–314. <https://doi.org/10.1007/BF00561842>
- Greeley, R. (1971b). *Observations of actively forming lava tubes and associated structures, Hawaii*. NASA technical memorandum X-62014. Retrieved from <https://ntrs.nasa.gov/archive/nasa/casi.ntrs.nasa.gov/19710009490.pdf>
- Greeley, R. (1972). Additional observations of actively forming lava tubes and associated structures, Hawaii. *Modern Geology*, 3, 157–160.
- Greeley, R. (1987). The role of lava tubes in Hawaiian volcanoes. *US Geologic Survey Professional Paper*, 1350(2), 1589–1602.
- Halliday, W. (1998). “Pit craters”, lava tubes, and open vertical volcanic conduits in Hawaii: A problem in terminology. *International Journal of Speleology*, 27(1), 113–124. <https://doi.org/10.5038/1827-806X.27.1.12>
- Haruyama, J., Hioki, K., Shirao, M., Morota, T., Hiesinger, H., van der Bogert, C. H., et al. (2009). Possible lunar lava tube skylight observed by SELENE cameras. *Geophysical Research Letters*, 36(21), L21206. <https://doi.org/10.1029/2009GL040635>
- Haruyama, J., Kaku, T., Shinoda, R., Miyake, W., Kumamoto, A., Ishiyama, K., et al. (2017). *Detection of lunar lava tubes by lunar radar sounder onboard SELENE* (Vol. 2).
- Head, J. W. (1976). Lunar volcanism in space and time. *Reviews of Geophysics*, 14(2), 265–300. <https://doi.org/10.1029/RG014i002p00265>
- Head, J. W., & Wilson, L. (2017). Generation, ascent and eruption of magma on the Moon: New insights into source depths, magma supply, intrusions and effusive/explosive eruptions (Part 2: Predicted emplacement processes and observations). *Icarus*, 283, 176–223. <https://doi.org/10.1016/j.icarus.2016.05.031>
- Hemingway, D. J., & Tikoo, S. M. (2018). Lunar swirl morphology constrains the geometry, magnetization, and origins of lunar magnetic anomalies. *Journal of Geophysical Research: Planets*, 123(8), 2223–2241. <https://doi.org/10.1029/2018JE005604>
- Hiesinger, H., Head, J. W., III, Wolf, U., Jaumann, R., & Neukum, G. (2010). Ages and stratigraphy of lunar mare basalts in Mare Frigoris and other nearside maria based on crater size-frequency distribution measurements. *Journal of Geophysical Research*, 115(E3), E03003. <https://doi.org/10.1029/2009JE003380>
- Hinze, W. J., Frese, R. R. B., von Frese, R. V., & Saad, A. H. (2013). *Gravity and magnetic exploration: Principles, practices, and applications*. Cambridge University Press. <https://doi.org/10.1017/cbo9780511843129>
- Hinze, W. J., Hood, P. J., Bonini, W. E., Case, J. E., de la Fuente, M., Godson, R. H., et al. (1998). Magnetic anomaly map of North America. *Geophysics: The Leading Edge of Exploration*, 7(11), 19–21. <https://doi.org/10.1190/1.1439458>
- Hon, K., Kauahikaua, J., Denlinger, R., & Mackay, K. (1994). Emplacement and inflation of pahoehoe sheet flows: Observations and measurements of active lava flows on Kilauea Volcano, Hawaii. *The Geological Society of America Bulletin*, 106(3), 351–370. [https://doi.org/10.1130/0016-7606\(1994\)106<0351:EAIOPS>2.3.CO;2](https://doi.org/10.1130/0016-7606(1994)106<0351:EAIOPS>2.3.CO;2)
- Hood, L. L., Zakharian, A., Halekas, J., Mitchell, D. L., Lin, R. P., Acuña, M. H., & Binder, A. B. (2001). Initial mapping and interpretation of lunar crustal magnetic anomalies using Lunar Prospector magnetometer data. *Journal of Geophysical Research*, 106(E11), 27825–27839. <https://doi.org/10.1029/2000JE001366>
- Horz, F. (1985). Lava tubes: Potential shelters for habitats. In *Lunar bases and space activities of the 21st century* (1st ed., pp. 405–412). Lunar and Planetary Institute. Retrieved from https://www.lpi.usra.edu/publications/books/lunar_bases/FrontMatter.pdf

- Hurwitz, D. M., Head, J. W., & Hiesinger, H. (2013). Lunar sinuous rilles: Distribution, characteristics, and implications for their origin. *Planetary and Space Science*, 79(80), 1–38. <https://doi.org/10.1016/j.pss.2012.10.019>
- Jawin, E. R., Valencia, S. N., Watkins, R. N., Crowell, J. M., Neal, C. R., & Schmidt, G. (2019). Lunar science for landed missions workshop findings report. *Earth and Space Science*, 6(1), 2–40. <https://doi.org/10.1029/2018EA000490>
- Kaku, T., Haruyama, J., Miyake, W., Kumamoto, A., Ishiyama, K., Nishibori, T., et al. (2017). Detection of intact lava tubes at Marius Hills on the Moon by SELENE (Kaguya) Lunar Radar Sounder: Intact lunar lava tube detection by LRS. *Geophysical Research Letters*, 44(20), 10155–10161. <https://doi.org/10.1002/2017GL074998>
- Keszthelyi, L. (1995). A preliminary thermal budget for lava tubes on the Earth and planets. *Journal of Geophysical Research*, 100(B10), 20411–20420. <https://doi.org/10.1029/95JB01965>
- Keszthelyi, L., & Self, S. (1998). Some physical requirements for the emplacement of long basaltic lava flows. *Journal of Geophysical Research*, 103(B11), 27447–27464. <https://doi.org/10.1029/98JB00606>
- Kiefer, W. S., Macke, R. J., Britt, D. T., Irving, A. J., & Consolmagno, G. J. (2012). The density and porosity of lunar rocks. *Geophysical Research Letters*, 39(7). <https://doi.org/10.1029/2012GL051319>
- Klitgord, K. D., Huestis, S. P., Mudie, J. D., & Parker, R. L. (1975). An analysis of near-bottom magnetic anomalies: Sea-floor spreading and the magnetized layer. *Geophysical Journal International*, 43(2), 387–424. <https://doi.org/10.1111/j.1365-246X.1975.tb00641.x>
- Kobayashi, T., Kim, J.-H., Lee, S. R., & Song, K.-Y. (2021). Nadir detection of lunar lava tube by Kaguya lunar radar sounder. *IEEE Transactions on Geoscience and Remote Sensing*, 59(9), 7395–7418. <https://doi.org/10.1109/TGRS.2020.3033033>
- Larson, C., & Larson, J. (1990). *Lava Beds Caves*. ABC Publishing.
- Mallozzi, A. (2019). *Magnetic and electromagnetic surveying of lava tubes at Lava Beds National Monument, California* (Master of Science). Carleton University. <https://doi.org/10.22215/etd/2019-13878>
- Marshall, A., Connor, C., Kruse, S., Malservisi, R., Richardson, J., Courtland, L., et al. (2015). Subsurface structure of a maar–diatreme and associated tuff ring from a high-resolution geophysical survey, Rattlesnake Crater, Arizona. *Journal of Volcanology and Geothermal Research*, 304, 253–264. <https://doi.org/10.1016/j.jvolgeores.2015.09.006>
- Meglich, T. M., Williams, M. C., Hodges, S. M., & DeMarco, M. J. (2003). *Subsurface geophysical imaging of lava tubes* (Vol. 13). Lava Beds National Monument.
- Minty, B. R. S., Milligan, P. R., Luyendyk, T., & Mackey, T. (2003). Merging airborne magnetic surveys into continental-scale compilations. *Geophysics*, 68(3), 988–995. <https://doi.org/10.1190/1.1581070>
- Miyamoto, H., Haruyama, J., Kobayashi, T., Suzuki, K., Okada, T., Nishibori, T., et al. (2005). Mapping the structure and depth of lava tubes using ground penetrating radar. *Geophysical Research Letters*, 32(21), L21316. <https://doi.org/10.1029/2005GL024159>
- Nagata, T., Fisher, R. M., & Schwerer, F. C. (1974). Some characteristic magnetic properties of lunar materials. *The Moon*, 9(1–2), 63–77. <https://doi.org/10.1007/BF00565393>
- National Geophysical Data Center. (2020). *National Centers for Environmental Information Geomagnetic Calculators*. Retrieved from <https://www.ngdc.noaa.gov/geomag/calculators/magcalc.shtml#igrfwmm>
- Negro, C. D., & Ferrucci, F. (1998). Magnetic history of a dyke on Mount Etna (Sicily). *Geophysical Journal International*, 133(2), 451–458. <https://doi.org/10.1046/j.1365-246X.1998.00517.x>
- Peterson, D., Holcomb, R., Tilling, R., & Christiansen, R. (1994). *Development of lava tubes in the light of observations at Mauna Ulu, Kilauea Volcano, Hawaii*, 56(5), 343–360. <https://doi.org/10.1007/bf00326461>
- Peterson, D. W., & Swanson, D. A. (1974a). *Observed formation of lava tubes.pdf*.
- Peterson, D. W., & Swanson, D. A. (1974b). Observed formation of lava tubes during 1970–71 at Kilauea Volcano, Hawaii. *Studies in Speleology*, 2(6), 209–222.
- Pieri, D. C., & Baloga, S. M. (1986). Eruption rate, area, and length relationships for some Hawaiian lava flows. *Journal of Volcanology and Geothermal Research*, 30(1–2), 29–45. [https://doi.org/10.1016/0377-0273\(86\)90066-1](https://doi.org/10.1016/0377-0273(86)90066-1)
- Piombo, A., Di Bari, M., Tallarico, A., & Dragoni, M. (2016). Thermal anomaly at the Earth's surface associated with a lava tube. *Journal of Volcanology and Geothermal Research*, 325, 148–155. <https://doi.org/10.1016/j.jvolgeores.2016.06.019>
- Ravat, D., Purucker, M. E., & Olsen, N. (2020). Lunar magnetic field models from Lunar Prospector and SELENE/Kaguya along-track magnetic field gradients. *Journal of Geophysical Research: Planets*, 125(7), e2019JE006187. <https://doi.org/10.1029/2019JE006187>
- Roberts, C. E., & Gregg, T. K. P. (2019). Rima Marius, the Moon: Formation of lunar sinuous rilles by constructional and erosional processes. *Icarus*, 317, 682–688. <https://doi.org/10.1016/j.icarus.2018.02.033>
- Robinson, M. S., Ashley, J. W., Boyd, A. K., Wagner, R. V., Speyerer, E. J., Ray Hawke, B., et al. (2012). Confirmation of sublunarean voids and thin layering in mare deposits. *Planetary and Space Science*, 69(1), 18–27. <https://doi.org/10.1016/j.pss.2012.05.008>
- Runcorn, S. K., Collinson, D. W., O'Reilly, W., Stephenson, A., Greenwood, N. N., & Battey, M. H. (1970). Magnetic properties of lunar samples. *Science*, 167(3918), 697–699. <https://doi.org/10.1126/science.167.3918.697>
- Sakimoto, S. E. H., Crisp, J., & Baloga, S. M. (1997). Eruption constraints on tube-fed planetary lava flows. *Journal of Geophysical Research*, 102(E3), 6597–6613. <https://doi.org/10.1029/97JE00069>
- Sauro, F., Pozzobon, R., Massironi, M., De Berardinis, P., Santagata, T., & De Waele, J. (2020). Lava tubes on Earth, Moon and Mars: A review on their size and morphology revealed by comparative planetology. *Earth-Science Reviews*, 209, 103288. <https://doi.org/10.1016/j.earscirev.2020.103288>
- Self, S., Thordarson, T., Keszthelyi, L., Walker, G. P. L., Hon, K., Murphy, M. T., et al. (1996). A new model for the emplacement of Columbia River basalts as large, inflated pahoehoe lava flow fields. *Geophysical Research Letters*, 23(19), 2689–2692. <https://doi.org/10.1029/96GL02450>
- Sigurdsson, H., Houghton, B., McNutt, S., Rymer, H., & Stix, J. (2015). *The encyclopedia of volcanoes*. Elsevier.
- Sobel, I. (2014). *History and definition of the sobel operator*. Retrieved from https://www.researchgate.net/publication/239398674_An_Isotropic_3x3_Image_Gradient_Operator
- Srnka, L. J., Hoyt, J. L., Harvey, J. V. S., & McCoy, J. E. (1979). A study of the Rima Sirsalis lunar magnetic anomaly. *Physics of the Earth and Planetary Interiors*, 20(2–4), 281–290. [https://doi.org/10.1016/0031-9201\(79\)90051-7](https://doi.org/10.1016/0031-9201(79)90051-7)
- Strauss, B. E., Tikoo, S. M., Gross, J., Setera, J. B., & Turrin, B. (2021). Constraining the decline of the lunar dynamo field at ≈ 3.1 Ga through paleomagnetic analyses of Apollo 12 mare basalts. *Journal of Geophysical Research: Planets*, 126(3), e2020JE006715. <https://doi.org/10.1029/2020JE006715>
- Tikoo, S. M., Weiss, B. P., Shuster, D. L., Suavet, C., Wang, H., & Grove, T. L. (2017). A two-billion-year history for the lunar dynamo. *Science Advances*, 3(8), e1700207. <https://doi.org/10.1126/sciadv.1700207>
- Titus, T. N., Wynne, J. J., Malaska, M. J., Agha-Mohammadi, A., Buhler, P. B., Alexander, E. C., et al. (2021). A roadmap for planetary caves science and exploration. *Nature Astronomy*, 5(6), 524–525. <https://doi.org/10.1038/s41550-021-01385-1>

- Tsunakawa, H., Shibuya, H., Takahashi, F., Shimizu, H., Matsushima, M., Matsuoka, A., et al. (2010). Lunar magnetic field observation and initial global mapping of lunar magnetic anomalies by MAP-LMAG onboard SELENE (Kaguya). *Space Science Reviews*, 154(1–4), 219–251. <https://doi.org/10.1007/s11214-010-9652-0>
- Tsunakawa, H., Takahashi, F., Shimizu, H., Shibuya, H., & Matsushima, M. (2015). Surface vector mapping of magnetic anomalies over the Moon using Kaguya and Lunar Prospector observations. *Journal of Geophysical Research: Planets*, 120(6), 1160–1185. <https://doi.org/10.1002/2014JE004785>
- Wagner, R., & Robinson, M. (2021). 2530.pdf. *Occurrence and origin of lunar pits: Observations from a new catalog* (Vol. 2548). Retrieved from <https://www.hou.usra.edu/meetings/lpsc2021/pdf/2530.pdf>
- Wagner, R. V., & Robinson, M. S. (2014). Distribution, formation mechanisms, and significance of lunar pits. *Icarus*, 237, 52–60. <https://doi.org/10.1016/j.icarus.2014.04.002>
- Walker, G. P. L. (1973). *Mount Etna and the 1971 eruption—Lengths of lava flows* (pp. 107–118). Philosophical Transactions of the Royal Society of London.
- Waters, A., Donnelly-Nolan, J., & Rogers, B. (2010). *Selected caves and lava-tube systems in and near Lava Beds National Monument, California* (Vol. 1673). U.S. Geological Survey Bulletin.
- Wendel, J. (2017). Lunar lava tubes could offer future Moon explorers a safe haven. *Eos, Transactions American Geophysical Union*, 98. <https://doi.org/10.1029/2017EO070477>
- Whelley, P., Garry, W. B., Young, K., Kruse, S., Esmaeili, S., Jazayeri, S., et al. (2018). Lidar surveys of lava tubes in Lava Beds National Monument. In *Presented at the Geologic Society of America annual Meeting, Indianapolis, Indiana*. <https://doi.org/10.1130/abs/2018AM-322466>
- Wieczorek, M. A., Weiss, B. P., & Stewart, S. T. (2012). An impactor origin for lunar magnetic anomalies. *Science*, 335(6073), 1212–1215. <https://doi.org/10.1126/science.1214773>
- Williams, D. A., O'Brien, D. P., Schenk, P. M., Denevi, B. W., Carsenty, U., Marchi, S., et al. (2014). Lobate and flow-like features on asteroid Vesta. *Planetary and Space Science*, 103, 24–35. <https://doi.org/10.1016/j.pss.2013.06.017>
- Wilson, L., & Keil, K. (1996). Volcanic eruptions and intrusions on the asteroid 4 Vesta. *Journal of Geophysical Research*, 101(E8), 18927–18940. <https://doi.org/10.1029/96JE01390>
- Xu, W., Van der Voo, R., Peacor, D. R., & Beaubouef, R. T. (1997). Alteration and dissolution of fine-grained magnetite and its effects on magnetization of the ocean floor. *Earth and Planetary Science Letters*, 151(3–4), 279–288. [https://doi.org/10.1016/S0012-821X\(97\)81854-7](https://doi.org/10.1016/S0012-821X(97)81854-7)
- Zhao, J., Huang, J., Kraft, M. D., Xiao, L., & Jiang, Y. (2017). Ridge-like lava tube systems in southeast Tharsis, Mars. *Geomorphology*, 295, 831–839. <https://doi.org/10.1016/j.geomorph.2017.08.023>